Monthly Notices of the ROYAL ASTRONOMICAL SOCIETY

MNRAS **459,** 820–840 (2016) doi:10.1093/mnras/stw592
Advance Access publication 2016 March 14

Compact symmetric objects and supermassive binary black holes in the VLBA Imaging and Polarimetry Survey

S. E. Tremblay,[1,2,3★] G. B. Taylor,[1,4] A. A. Ortiz,[1] C. D. Tremblay,[2] J. F. Helmboldt[5] and R. W. Romani[6]

[1]*Department of Physics and Astronomy, University of New Mexico, Albuquerque, NM 87131, USA*
[2]*International Centre for Radio Astronomy Research (ICRAR), Curtin University, Bentley, WA 6102, Australia*
[3]*ARC Centre of Excellence for All-sky Astrophysics (CAASTRO), Sydney, Australia*
[4]*National Radio Astronomy Observatory, Socorro NM 87801, USA*
[5]*Naval Research Laboratory, Code 7213, Washington, DC 20375, USA*
[6]*Department of Physics, Stanford University, Stanford, CA 94305, USA*

Accepted 2016 March 9. Received 2016 March 8; in original form 2016 January 22

ABSTRACT

We present multifrequency Very Long Baseline Array (VLBA) follow-up observations of VLBA Imaging and Polarimetry Survey sources identified as likely compact symmetric objects (CSOs) or supermassive binary black holes (SBBHs). We also present new spectroscopic redshifts for 11 sources observed with the Hobby–Eberly Telescope. While no new SBBHs can be confirmed from these observations, we have identified 24 CSOs in the sample, 15 of which are newly designated, and refuted 52 candidates leaving 33 unconfirmed candidates. This is the first large uniform sample of CSOs which can be used to elicit some of the general properties of these sources, including morphological evolution and environmental interaction. We have detected polarized emission from two of these CSOs the properties of which are consistent with active galactic nuclei unification schemes.

Key words: galaxies: active – galaxies: evolution – galaxies: jets – galaxies: nuclei – radio continuum: galaxies.

1 INTRODUCTION

In 2006, the Very Long Baseline Array (VLBA) performed a large full polarization survey of radio sources, the VLBA Imaging and Polarimetry Survey (VIPS; Helmboldt et al. 2007). This survey was comprised of 198 h of 5 GHz observations, targeting a subset of 1127 sources from the cosmic lens all-sky survey (CLASS; Myers et al. 2003). While the primary goal of the survey was to identify and characterize potential *Fermi Gamma-ray Space Telescope* sources (Linford et al. 2011), two concurrent objectives were to identify candidate members of two classes of rare astronomical objects, compact symmetric objects (CSOs) and supermassive binary black holes (SBBHs).

CSOs can broadly be described as dual-lobed sources whose extent is less than a kiloparsec and that are oriented close to the plane of the sky (Wilkinson et al. 1994). Similar to larger radio galaxies, the morphology we observe consists of relativistic jets emitted from opposing sides of the core, presumably where the central supermassive black hole resides. These jets then terminate at hotspots, where the fast moving jet material interacts with the surrounding media, intergalactic medium for large radio galaxies and interstellar medium for small CSOs, and inflate lobes. The emission of CSOs is typically dominated by these hotspots (Readhead et al. 1996), typically leading to edge brightening. Multi-epoch observations show the distance separating the furthest extents of the lobes typically increasing at ∼0.1 c (Taylor et al. 2000) which, when extracted backwards to estimate the ages of these sources, implies that CSOs are young, ranging from ∼20 to 2000 yr old (Gugliucci et al. 2005). The small size and orientation of these sources make CSOs ideal for studying both galactic evolution and the properties of the media surrounding the active galactic nuclei (AGN). Coupling this with the small number of heretofore confirmed CSOs, 50–90 (Augusto et al. 2006; Augusto 2009) justifies the further study of these objects. Furthermore, the confirmed CSOs to date have mostly resulted from targeted observations aimed at a high rate of confirmation resulting in a lack of understanding in how these objects fit into our general understanding of AGN, which a large sample of CSOs found within a uniform sample could provide.

The combined theories of galactic growth via mergers and the residence of supermassive black holes in the centres of most galaxies necessitate supermassive black hole interactions if both are correct (Merritt & Milosavljević 2005). Binary black holes, which themselves end either in a merger event or ejection, are a naturally expected outcome of these interactions. The observed correlation between central supermassive black hole mass and the mass of the

★ E-mail: steven.tremblay@curtin.edu.au

stellar bulge in galaxies (Magorrian et al. 1998; Kormendy & Ho 2013; Graham & Scott 2015) further strengthens the expectation of binary systems. To date, the number of close separation ($\leq$10 pc) SBBH candidates is small with only 0402+379 having morphological verification (Rodriguez et al. 2006, 2009). One of the goals for this survey of over 1000 galaxies was to identify, and potentially confirm, new SBBH candidates.

This paper explores the follow-up observations performed on sources identified as either CSO or SBBH candidates. More detailed analysis, in particular on the individual sources comprising the VIPS CSO sample, will be carried out in a subsequent paper. Throughout this paper, we assume $H_0 = 73\,\mathrm{km\,s^{-1}\,Mpc^{-1}}$, $\Omega_\mathrm{m} = 0.27$, $\Omega_\Lambda = 0.73$, unless noted otherwise. This paper makes use of Ned Wright's Javascript Cosmology Calculator (Wright 2006).

2 SAMPLE SELECTION, OBSERVATIONS AND DATA REDUCTION

2.1 Sample selection

The sample selection is described in detail in Helmboldt et al. (2007). Here we outline the VIPS classification process to better understand the follow-up sample being studied in this paper.

After imaging, an automated morphological classification was performed on all 1127 VIPS sources. This started with the AIPS (Greisen 2003) task SAD being used to generate multicomponent Gaussian models for each source. The sources were then categorised as follows

(i) Sources with a single Gaussian component containing $\geq$95 per cent of the total flux density were flagged as single component sources.
(ii) Sources where the two brightest Gaussian components contained $\geq$95 per cent of the total flux density were flagged as double sources.
(iii) Sources that did not fit these criteria were flagged as multiple component sources.

These preliminary categories were then refined as follows.

(i) Single component sources with minor/major axis ratios of $>$0.6 were classified as point sources (PSs), otherwise they were flagged as core-jets (0.6 was chosen since this was the axis ratio of the restoring beam used in the VIPS images).
(ii) Double sources where the flux densities of the two brightest components match within a factor of 2.5 were classified as CSO candidates (CSOs).
(iii) Multiple components sources where the components containing $\geq$95 per cent of the total flux density were located along a single line were flagged as core-jets, otherwise they were classified as complex (CPLX).
(iv) Core-jets longer than 6 mas were classified as long jets (LJETs), otherwise they were placed in the category of short jets (SJETs).
(v) LJETs longer than 12 mas whose brightest Gaussian component was positioned within 3 mas of the centre of the structure were reclassified as CSO candidates (CSOs).

The two separate ways sources could be classified as CSO candidates were instituted since the jets connecting the hotspots and lobes of CSOs back to the core are sometimes, but not always, detectable. The automatic source classifications were then verified visually and false classifications corrected (87 per cent CSOs and 71 per cent CPLX sources were correct). This yielded 103 CSOs and 17 CPLX sources needing follow-up observations.

The list of SBBH candidates was generated by visually inspecting the 5 GHz images and looking for sources that appeared to have two distinct axes of emission, possibly indicating the existence of two separate bi-directional jet flows from two cores. The CPLX sources were included in the follow-up both because they were a good place to look for SBBHs and since non-archetypical CSOs can easily be classified as such.

2.2 Observations, calibration and imaging

2.2.1 Radio data

Two subsets of multifrequency observations of the candidates were performed. A series of four separate observing runs from 2006 September to 2007 February (BT088) and another five observing runs were performed from 2007 June to 2008 June (BT094) all with the VLBA. Each of these observations consisted of four 8 MHz wide intermediate frequencies (IFs) in the C, X and U bands with full polarization centred at: 4605.5, 4675.5, 4990.5, 5091.5, 8106.0, 8176.0, 8491.0, 8590.0, 14 902.5, 14 910.5, 15 356.5 and 15 364.5 MHz at an aggregate bit rate of 256 Mbps to maximize (u,v) coverage and sensitivity. When the data in each band were combined, the three central frequencies were: 4844.7, 8344.7, and 15 137.5 MHz. The BT088 observations had typical times on source of $\sim$38 min at *C* and *X* band and $\sim$116 min at *U* Band. For BT094, typical time on source was $\sim$10 min for *C* and *X* band and $\sim$32 min for *U* Band. The integrations for each source were spread out over approximately 10 h to maximize (u,v) coverage for the observations.

Most of the calibration and initial imaging of the data were carried out by automated AIPS and DIFMAP (Shepherd 1997) scripts similar to those used in reducing the VIPS 5 GHz survey data (Taylor et al. 2005; Helmboldt et al. 2007). To summarize, flagging of bad data and calibration were performed using the VLBA data calibration pipeline (Sjouwerman et al. 2005), while imaging was performed using DIFMAP scripts described in Taylor et al. (2005). Final images were inspected and manually improved using the DIFMAP program to attain the best fidelity possible. Part of the final imaging scripts for *C* and *U* bands involved running the DIFMAP command selfcal on the data starting with the clean-component model of the *X*-band data as the input model to help in aligning the source across all three frequencies. This creates a phase 'correction' to shift the entire map in a way that maximises the alignment of the bright components across the map. This is the same method described in Bietenholz et al. (1997), where they align the maps for different frequencies for spectral index analysis.

The four IFs for each observing band were treated separately in order to maximize (u,v) coverage. The average root-mean-square scatter of the baseline visibility amplitudes in the calibrated data were $\pm$18, $\pm$16, and $\pm$14 mJy for the *C*, *X*, and *U* bands, respectively, for BT088 and $\pm$25, $\pm$23, and $\pm$8 mJy for the *C*, *X*, and *U* bands, respectively, of BT094. The BT094 15 GHz scatter is notably lower because we combined the four IFs after fringe fitting and calibration (at the expense of (u,v) coverage) in order to compensate for the lower flux levels resulting from the steep spectrum of many of the sources. For the polarimetric analysis, the lower two and upper two IF pairs in each band were combined and imaged to maximize the sensitivity while retaining some 'in-band' frequency information.

Polarization calibration was carried out by first aligning the polarization angles of all four IFs, within each band, to the pixel

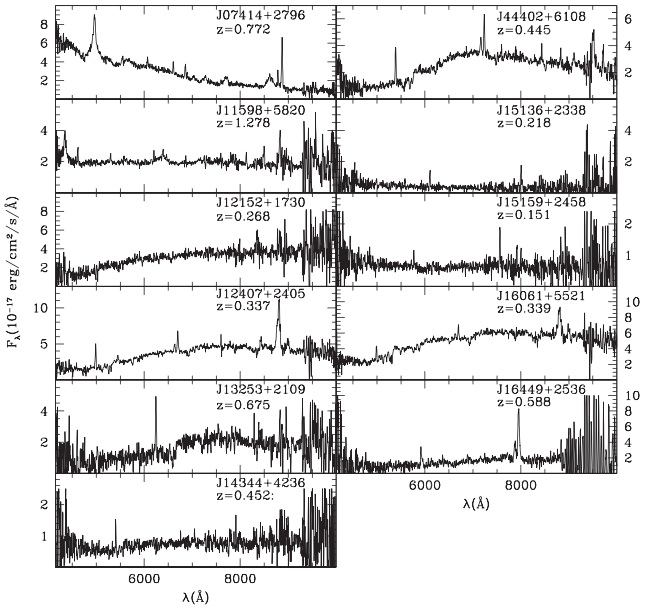

Figure 1. Optical spectra of CSOs with new redshifts from observing at the HET. All redshifts are confirmed from emission lines, although there remains some uncertainty in the redshift of J14344+4236. If the single strong line at 5406 Å towards J14344+4236 is identified as O II (3727 Å), then the redshift is $z = 0.5405$. This identification is supported by a substantial 4000 Å break, as well as weak detections of Ca H & K and Balmer features.

brightest in polarization for 3C279. Then, the mean polarization angles of J0854+2006 and J1310+3220 were compared to the values recorded in the VLA/VLBA Polarization Calibration Page[1] applying any necessary interpolations in either time or frequency. Typical errors in the electric vector polarization angle (EVPA) were 7°, 8°, and 13° for the 5, 8, and 15 GHz maps, respectively. This was determined using the deviation of the integrated EVPA across all three EVPA calibrators for each source.

2.2.2 *Optical data*

For a subset of our candidates (11 sources) which did not have published redshifts, spectroscopic observations were performed with the 9.2 m Hobby–Eberly Telescope (HET) at McDonald Observatory to obtain spectral redshifts. The HET observes in the declination range $-11^\circ < \delta < 73^\circ$ and is fully queue scheduled (Shetrone et al. 2007). We used the Marcario Low-Resolution Spectrograph (LRS; Hill et al. 1998), with grism G1 (300 lines mm^{-1}), a 2 arcsec slit, and a Schott GG385 long-pass filter for a resolution of R $\sim$ 500 between 4150 and 10 500 Å. Typical exposures were 2 $\times$ 900 s with the slit placed along the parallactic angle.

Data reduction was performed with the IRAF package (Tody 1986) using standard techniques. Wavelength calibration was performed with a neon-argon lamp. We employed an optimal extraction algorithm (Valdes 1992) to maximize the signal-to-noise ratio (S/N). We performed spectrophotometric calibration using standard stars from Oke (1990). Spectra were corrected for telluric absorptions and visually cleaned of cosmic rays. Multiple exposures on a single target were combined into a single spectrum, weighted by S/N. The resulting spectra can be seen in Fig. 1.

[1] http://www.vla.nrao.edu/astro/calib/polar/

3 RESULTS

3.1 Spectral index distribution

The 5 and 8 GHz, as well as the 8 and 15 GHz images were matched in resolution in order to obtain a spectral index distribution across the source, where we take $F_\nu \propto \nu^\alpha$. Each spectral index map was overlaid on to 5 GHz contours to understand the distribution of spectral index within each source structure (Figs 2–7). The spectral index maps for CSOs have been 'lettered' to facilitate discussion and referencing of the images, for the remaining maps for candidates and refuted CSOs the source name will be sufficient. For consistency, this analysis was automated using scripts which did the following.

(i) The resolution of the images was matched by first adding a (u, v) taper to the higher resolution maps until the beam was close (within roughly 0.03 mas for 5–8 GHz spectral index and 0.25 mas for 8–15 GHz spectral index) to the size of the lower frequency.

(ii) The beam size was then forced to match exactly using the DIFMAP command RESTORE, suppressing any residual large (u, v) values from the higher frequency. The map dimensions were also matched, then spectral index maps were made using the AIPS task COMB.

(iii) The Caltech package program MAPLOT was then used to overlay the spectral index maps on to the 5 GHz contours to identify where the spectral characteristics were located within the overall structure of each source.

Error maps associated with each spectral index map were produced using the root-mean-square error of the two input maps. In all these maps, the pixels on the edge of each feature have a higher error than the centre of the features since the border features are not sampled by the full synthesized beam. The average error in α for the maps, calculated by measuring the root mean square of the central features and the boundary of the components separately, are ±0.03, ±0.15 and ±0.03, ±0.14 for the 5–8 and 8–15 spectral index maps from BT088 and ±0.03, ±0.15 and ±0.04, ±0.13 for the 5–8 and 8–15 spectral index maps from BT094 respectively. This means that variation of that amplitude, particularly on size scales smaller than the beam width, should not be interpreted as realistic features on these maps.

3.2 VLBI recovery of flux density

Comparing the summed flux densities of the CSOs at each frequency (Table 1) with the previously observed flux densities from surveys at single dish and shorter baseline interferometers (i.e. VLSS, WENSS, NVSS, GB6) we can test whether or not any emission is being missed by the VLBA observations. Sources could resolve out in these high-resolution observations if emission is on larger scales that is visible to the single dish, but not to the VLBA. In general, the agreement is excellent (Fig. 8). When compared to the 5 GHz single-dish observations of Becker, White & Edwards (1991), half of the sources recover the total flux within the formal errors and 21 sources agree within an additional 15 per cent. The few exceptions (J09062+4636, J12043+5202, and J12201+2916) could be the result of variability since there is a 15 yr separation between the observations.

Most of the CSOs exhibit a peak in these spectral energy distributions (SEDs) at $\sim$1 GHz, as expected for lobe dominated emission on size scales of $\sim$10 mas (O'Dea 1998). A second turnover, such as that hinted at in the SED for J12201+2916 below 300 MHz (Fig. 8), is indicative of larger scale (older) emission not

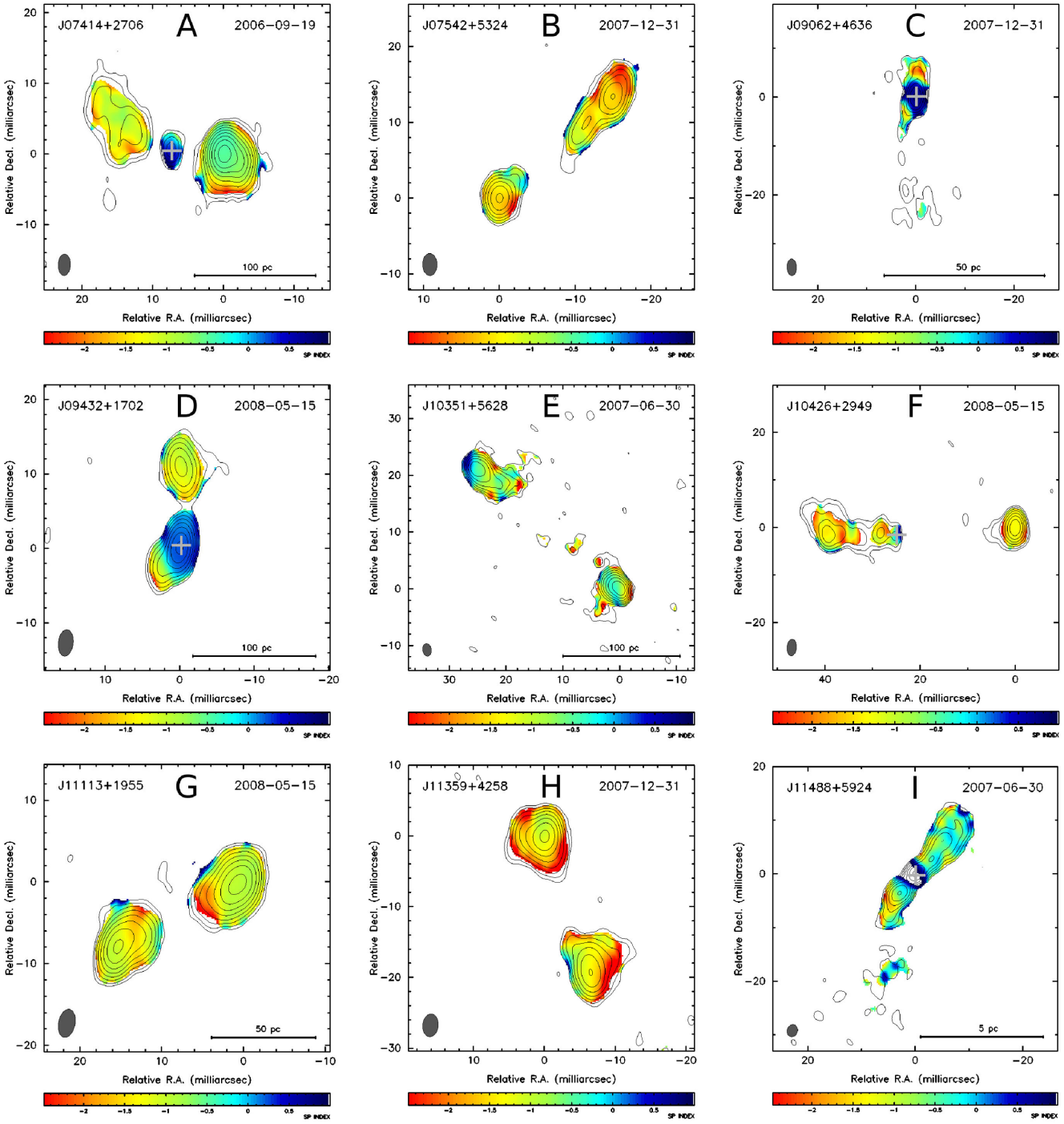

Figure 2. 5 GHz contour maps of VIPS CSOs with 5–8 GHz spectral index map overlays. The contour levels begin at thrice the theoretical noise (typically ∼ 0.4 mJy for BT088 and 1.0 mJy for BT094) and increases by powers of 2. The colour scale is fixed from −2.5 to 1 to facilitate comparison. When detected, a grey cross is placed over the core to guide the reader's eye. Sources with confirmed spectral redshifts have associated distance bars for linear scale.

associated with the younger radio source shown in Figs 2 and 3. Finally, it is worth pointing out that a few sources, notably J09062+4636, J12545+1856, J13113+1658, and J16449+2536, lack a clear peak. Since Fig. 8 contains only confirmed CSOs, this illustrates the point that not all CSOs necessarily have a gigahertz peaked spectrum (GPS) though most (82 per cent or 18 of 22) do. The GPS peak tells us about the dominant component size, but does not directly confirm a CSO nature or a young age for a given source.

3.3 Polarization

Polarimetric analysis was performed on all of the confirmed VIPS CSOs, and polarized flux was observed in two of the sources. J07414+2706 exhibited polarized emission at both 5 and 8 GHz and J13262+395 was detected in polarization at 8 and 15 GHz (see Figs 9 and 10). Polarized emission from non-CSOs will be presented in a future work, with the notable exception of J16021+3326,

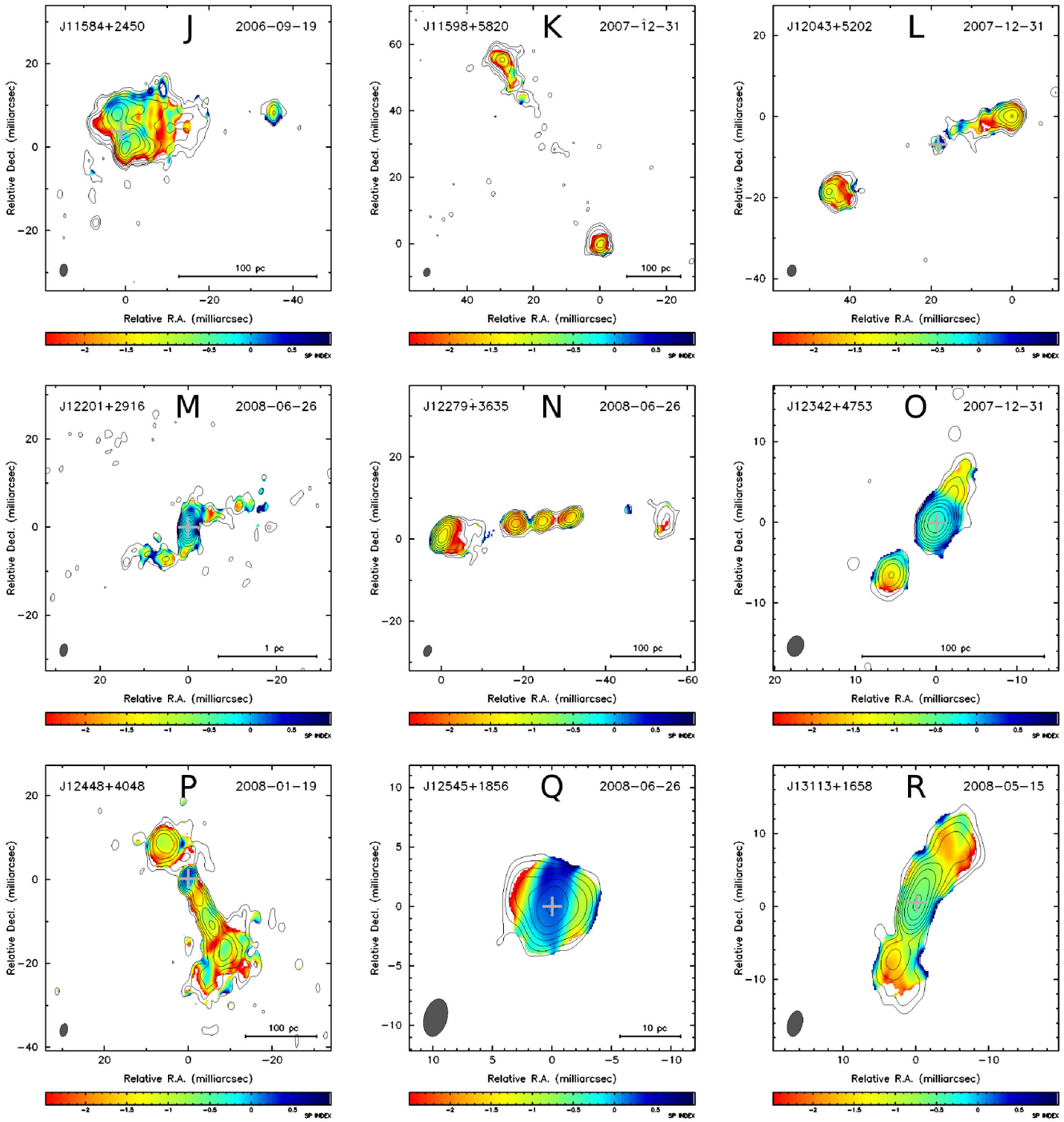

Figure 2 – (*Continued*).

whose polarization properties were investigated in the process of classifying it as a core-jet (Tremblay et al. 2010).

4 DISCUSSION

4.1 Definition of a CSO

Historically, the definition of a CSO has not been standardized and what one paper considers a requirement, another instead considers a common characteristic. We have adopted a broad definition for a CSO, keeping the term an observation-based definition allowing that this classification might encompass multiple physically distinct species. Even so, we suggest that the CSO category is more focused and relevant classification than the purely spectral classification of Gigahertz-peaked spectrum and Compact steep spectrum sources which are highly contaminated with blazars (Tornikoski et al. 2009).

We define a CSO as a source less than 1 kpc in projected extent, where two well-defined hotspots (the working surface where the jets push against the surrounding medium) and/or lobes (cavities filled with back flowing material) are observed, which is the

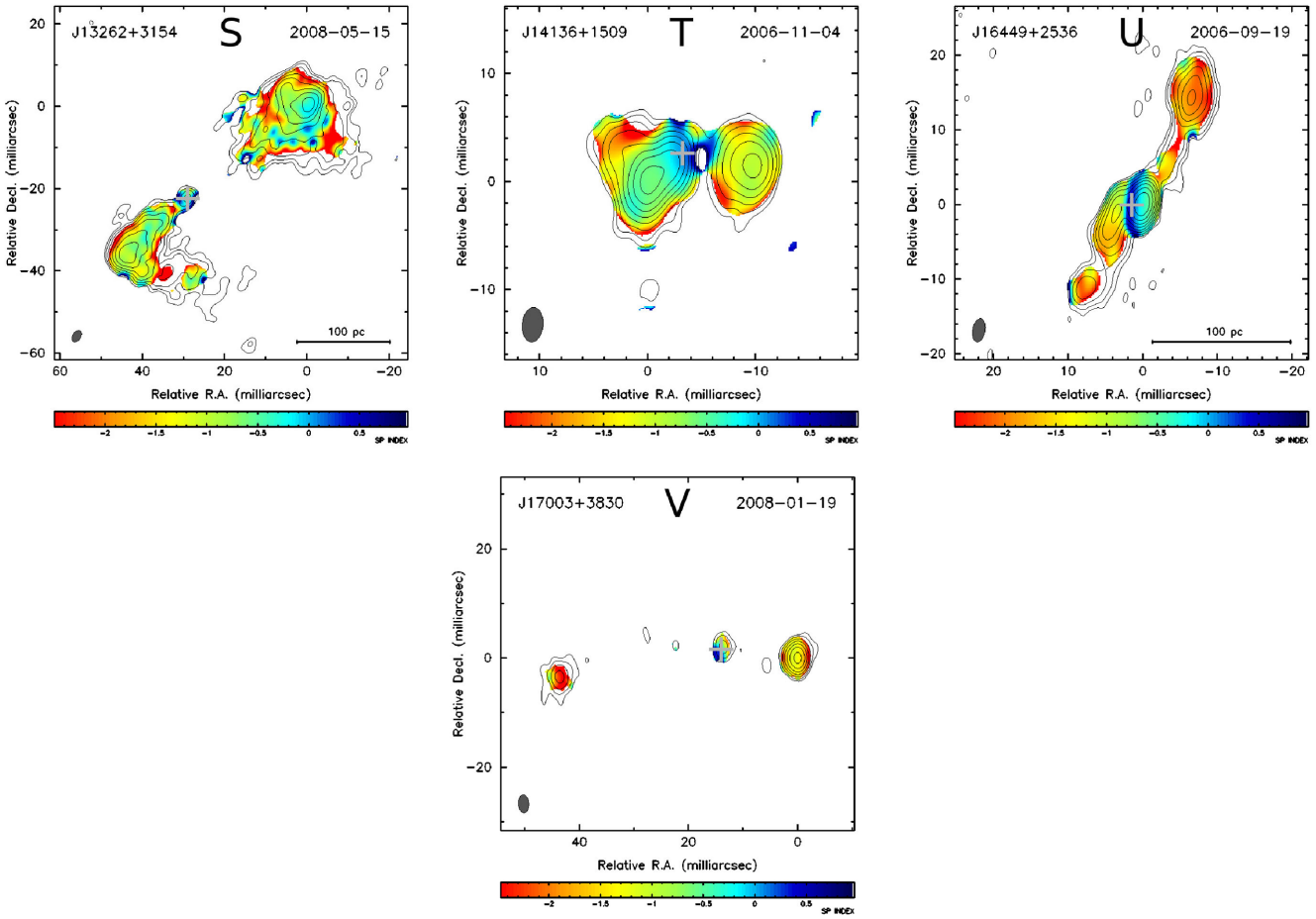

Figure 2 – (*Continued*).

simplest and most encompassing definition we can devise. Although the detection of a core is not strictly required, it does provide confirmation of the CSO identification and aids in the understanding the underlying geometry of these systems. The hotspots in these sources are typically discernible as being steep gradients at the ends of the lobes, a characteristic referred to as edge brightening. Several of the candidates in which counter jet/lobe emission was observed were still classified as non-CSOs (J08170+1958, J12035+4632, J12582+5421, J13128+5548 & J15159+2458); the *X*-band detection of the counter emission of these sources was 3σ or less. We decided these were most likely core-jets oriented at a large enough angle out of the plane of the sky to just detect the de-boosted counter-emission. Lower frequency VLBI observations could reveal them to have structure consistent with CSOs.

4.2 Confirmed CSOs

Here each of the 24 confirmed VIPS CSO will be briefly discussed. The properties of these CSOs are reported in Table 1 and spectral index maps of each source are in Figs 2 and 3.

4.2.1 J07414+2706

A flat-spectrum compact core is visible in both Figs 2(A) and 3(A) with lobes to the east and west. The western lobe is appreciably brighter than its counterpart due either to geometry or interaction with the surrounding media. Polarization is detected in the western lobe in both *X* and *U* bands (Fig. 10). This source has the highest flux density ratio for the two lobes (19.35), indicating either one side of this source is strongly interacting with its environment or the jets might not be as close to the plane of the sky as is usually assumed in a CSO. This source is ∼200 pc across at its largest extant.

4.2.2 J07542+5324

This source is comprised of lobes extending to the north-west and southeast (Fig. 2B). While the southern lobe shows flatting of its spectrum towards the centre of the system, there was not enough evidence to identify a component to associate with the core of the system. The *U*-band emission from this source was only marginally detected, and did not allow the generation of an accurate 8–15 GHz spectral index map. This source is also part of the CSOs Observed In the Northern Sky (COINS; Peck & Taylor 2000) project, where it was previously confirmed as a CSO.

4.2.3 J09062+4636

This source was strongly detected at all three frequencies and is comprised of an unresolved core with weak extension to the north and south (Figs 2C and 3C). We note the lack of edge brightening of the extended emission from this source that is typical of CSOs and is

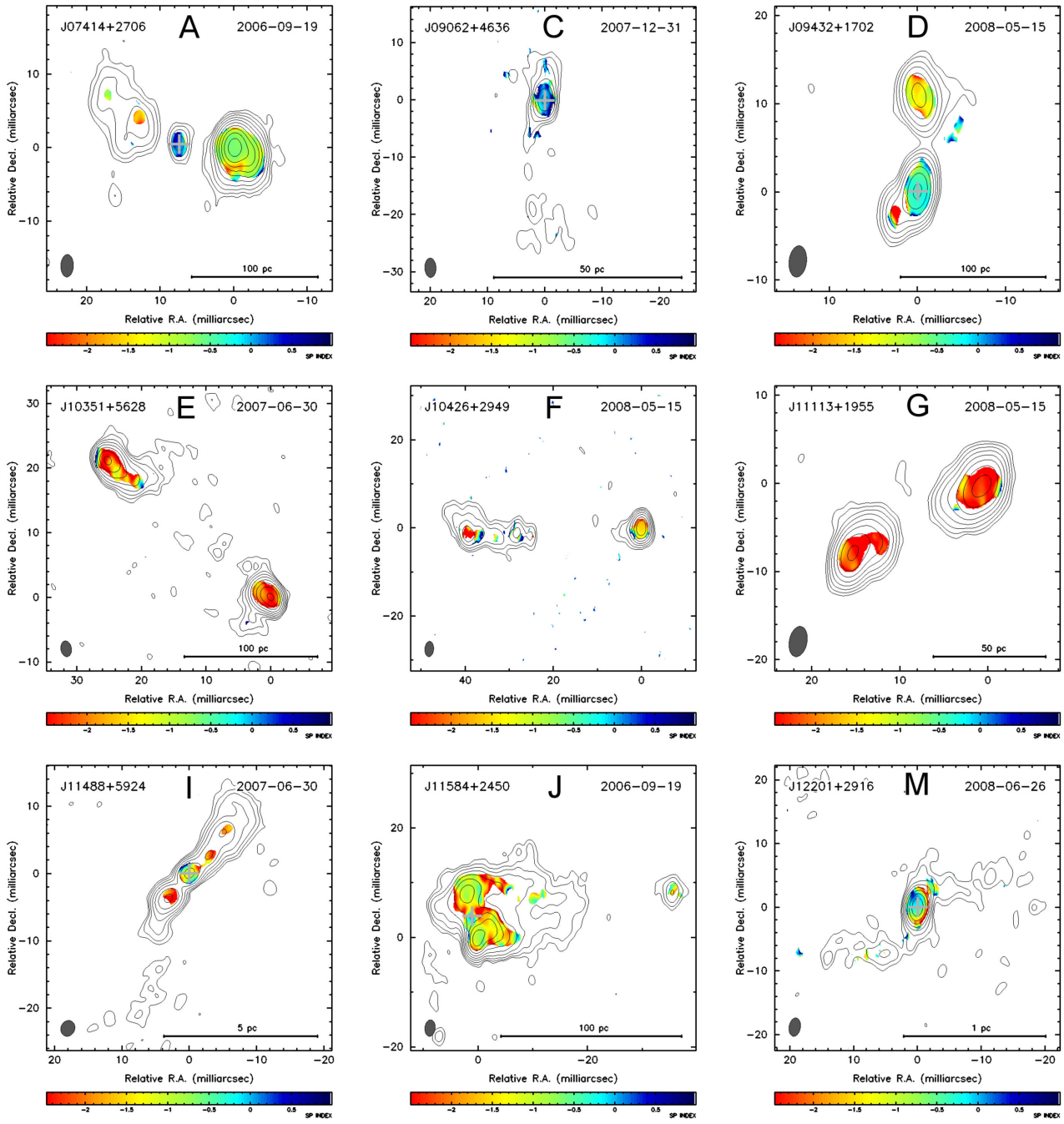

Figure 3. 5 GHz contour maps of VIPS CSOs with 8–15 GHz spectral index map overlays. The contour levels begin at thrice the theoretical noise (typically $\sim$ 0.4 mJy for BT088 and 1.0 mJy for BT094) and increases by powers of 2. The colour scale is fixed from -2.5 to 1 to facilitate comparison. When detected, a grey cross is placed over the core to guide the reader's eye. Sources with confirmed spectral redshifts have associated distance bars for linear scale.

instead characterized with FR-I-like morphology. Weak polarization was detected at 8 GHz, but no rotation measures could be calculated. This source was confirmed as a CSO by the Compact Radio Sources at Low Redshift (CORALZ; Snellen et al. 2004; de Vries et al. 2009) project.

4.2.4 J09432+1702

The brightest feature of this source at 5 GHz appears to be a flat-spectrum core (Figs 2D and 3D). The core ($\alpha \sim -1$ to -1.5) is edge brightened on its northeastern side. A small steep-spectrum protrusion to the south-east of the core is similarly brightened on its south-eastern side. This approximately 125 pc source is first identified as a CSO here in this paper and no other morphological studies have been conducted.

4.2.5 J10351+5628

This 188 pc source contains two steep-spectrum oppositely edge-brightened features (Figs 2E and 3E). While no obvious core was

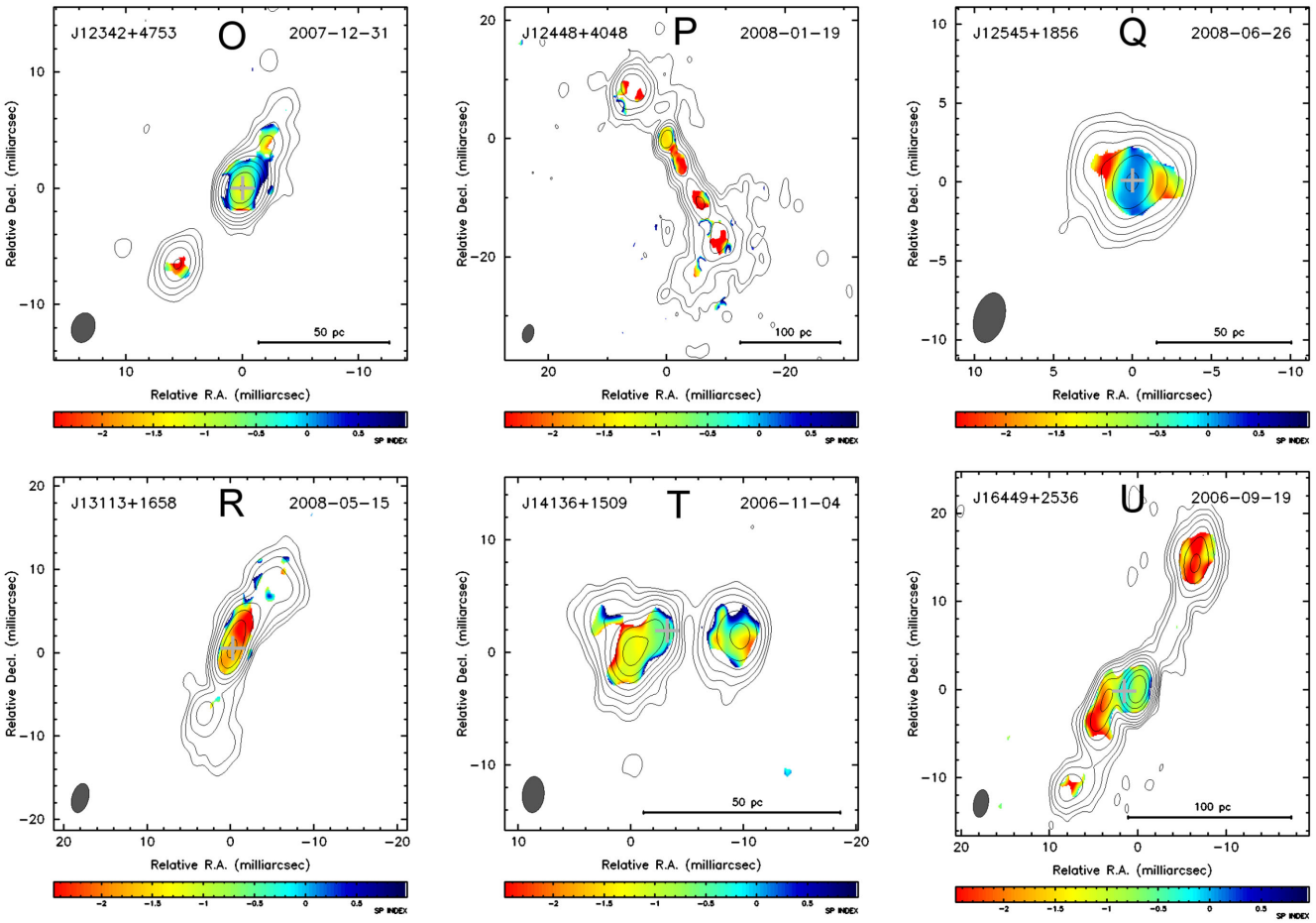

Figure 3 – (*Continued*).

observed, the morphology of this double system is convincingly that of a CSO. In Fig. 2(E), there are small (< the beam width) edge effects apparent (positive stripe on the east and negative stripe on the west), which most likely arise from a slight misalignment of the two frequencies due to the complicate spectral nature of the north-eastern lobe. This source was confirmed as a CSO in COINS (Peck & Taylor 2000).

4.2.6 J10426+2949

The two lobes of this source are comprised of bright, steep-spectrum, resolved components (Figs 2F and 3F). The eastern component is connected to extended emission tracing back towards the west, and ending in a faint, flat-spectrum component tentatively classified as the core. Automated images generated by the FIRST (Becker, White & Helfand 1995) and the NVSS (Condon et al. 1998) surveys both hint at possible extension to the north-west on kiloparsec scales suggesting a possible earlier epoch of emission.

4.2.7 J11113+1955

The two steep-spectrum structures within this source feature opposing brightened edges (Figs 2G and 3G). The morphology of this source is indicative enough to classify it as a CSO even though no core was observed. It is possible the very steep spectrum ($\alpha < -2$) observed in Fig. 3 is an artefact of the 15 GHz flux being near the detection threshold. This source was confirmed as a CSO in COINS (Peck & Taylor 2000).

4.2.8 J11359+4258

This source is characterized by symmetric, edge-brightened, steep-spectrum lobes that are consistent with CSO morphology (Fig. 2H). While the core is not apparent from these observations, and the redshift for this source is unknown, based on the structure we are classifying this source as a CSO.

4.2.9 J11488+5924

This source is characterized by a flat-spectrum core with diffuse lobes extending to the north-west and southeast (Figs 2I and 3I). This is a previously known nearby low-power CSO (Taylor, Wrobel & Vermeulen 1998; Peck & Taylor 2000). The apparently missing spectral information in Fig. 2(I) is due to the core of this source having a strongly inverted spectral index ($\alpha \sim 1$–1.5) between 5 and 8 GHz, which 'runs off' the right side of the spectral index scale whose values were fixed to maximize information content across all sources. This inversion is not steep enough to substantiate free–free absorption alone, as would be the case if we observed $\alpha \sim 4$–5. The low power ($L_{5\,\mathrm{GHz}} \sim 1 \times 10^{23}$) and the lack of edge brightening of this well-studied source could make it the prototype

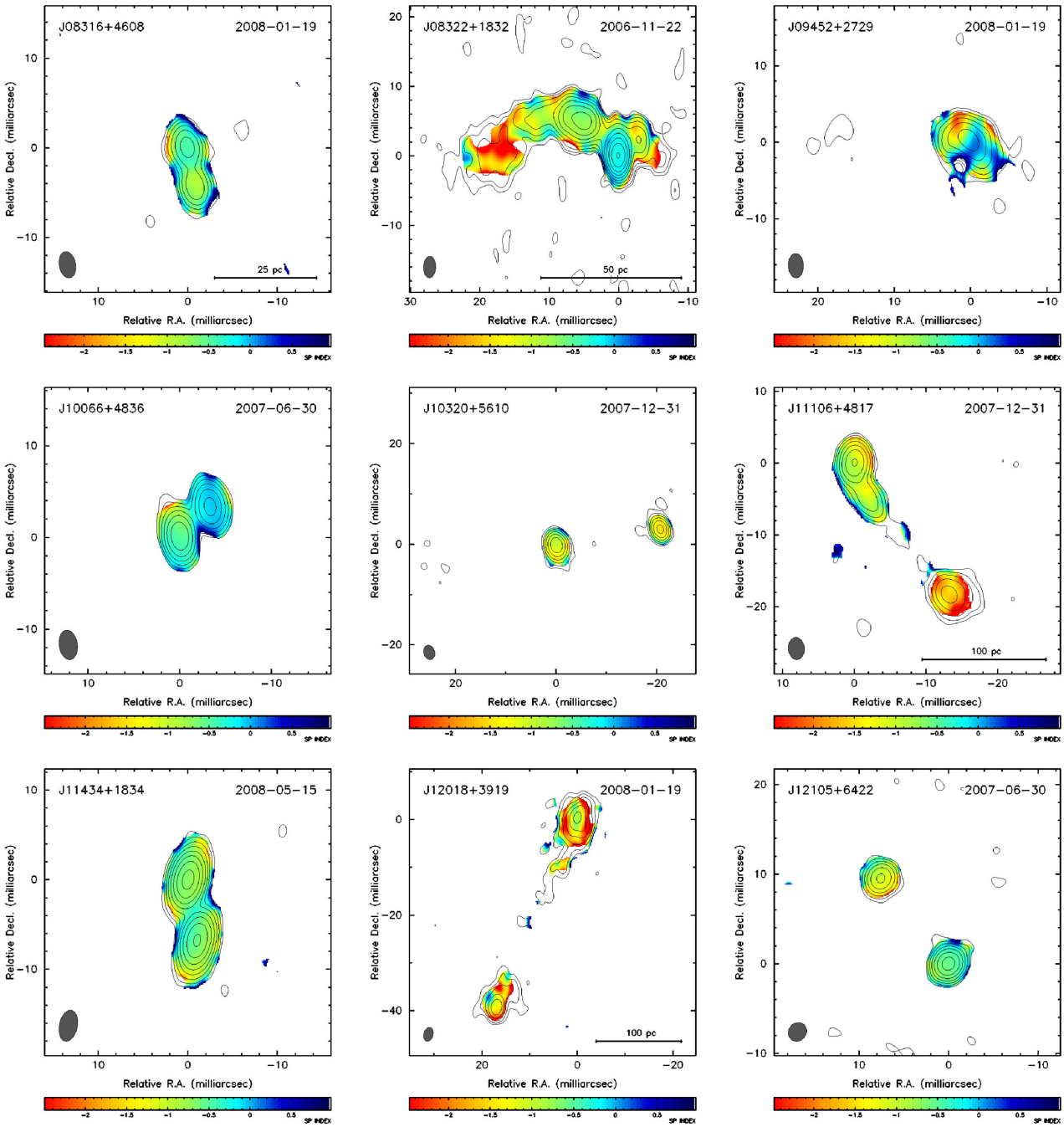

Figure 4. 5 GHz contour maps of the remaining CSO candidates with 5–8 GHz spectral index map overlays. The contour levels begin at thrice the theoretical noise (typically ~ 0.4 mJy for BT088 and 1.0 mJy for BT094) and increases by powers of 2. The colour scale is fixed from -2.5 to 1 to facilitate comparison. Sources with confirmed spectral redshifts have associated distance bars for linear scale. [The complete figure is available online.]

for CSOs with FR-I-like properties. This source is confirmed as a CSO in COINS (Peck & Taylor 2000).

4.2.10 J11584+2450

The flat-spectrum compact core has lobes extending to the north and south which is most easily seen in Fig. 3(J), although Fig. 2(J) highlights the complicated nature of this radio galaxy. These lobes then appear to sweep back and connect with the extended emission to the west. A very unusual CSO which seems to be interacting with its environment. See Tremblay et al. (2008) for deeper analysis and discussion of this interesting source.

4.2.11 J11598+5820

The lobes of this 515 pc size source are extended, steep-spectrum components with evidence of edge brightening at opposing edges (Fig. 2K). There is no easily identified core observed but the supporting morphological structure is strong enough evidence to classify it as a CSO.

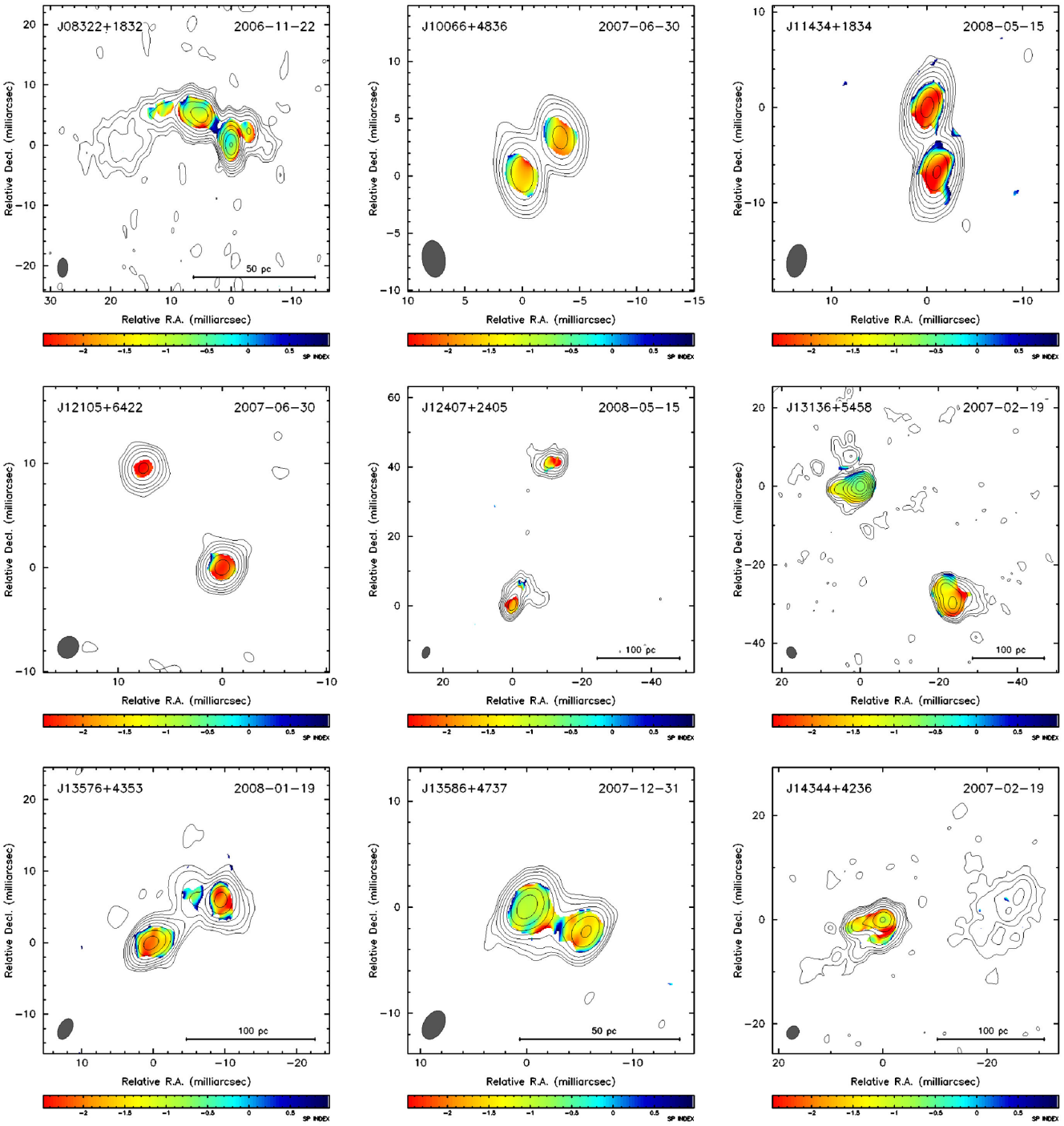

Figure 5. 5 GHz contour maps of the remaining CSO candidates with 8–15 GHz spectral index map overlays. The contour levels begin at thrice the theoretical noise (typically $\sim$ 0.4 mJy for BT088 and 1.0 mJy for BT094) and increases by powers of 2. The colour scale is fixed from -2.5 to 1 to facilitate comparison. Sources with confirmed spectral redshifts have associated distance bars for linear scale. [The complete figure is available online.]

4.2.12 J12043+5202

This source has a compact, flat-spectrum core with edge-brightened, steep-spectrum hotspots to the north-west and south-east (Fig. 2L). This source is an excellent example of the classic CSO morphology and this paper is the first to identify it as such. This is the only example, in our sample, of a CSO where the brightest hotspot is much closer to the core than its counterpart (Table 1) while all three components (the core and both hotspots) lie on an approximately straight line. If environmental interaction is the cause of the arm ratio, one might reasonably expect to see a deviation in the geometry which we do not observe.

4.2.13 J12201+2916

The dominant bright, flat-spectrum component is identified as the core (Figs 2M and 3M). From the north and south ends of the core,

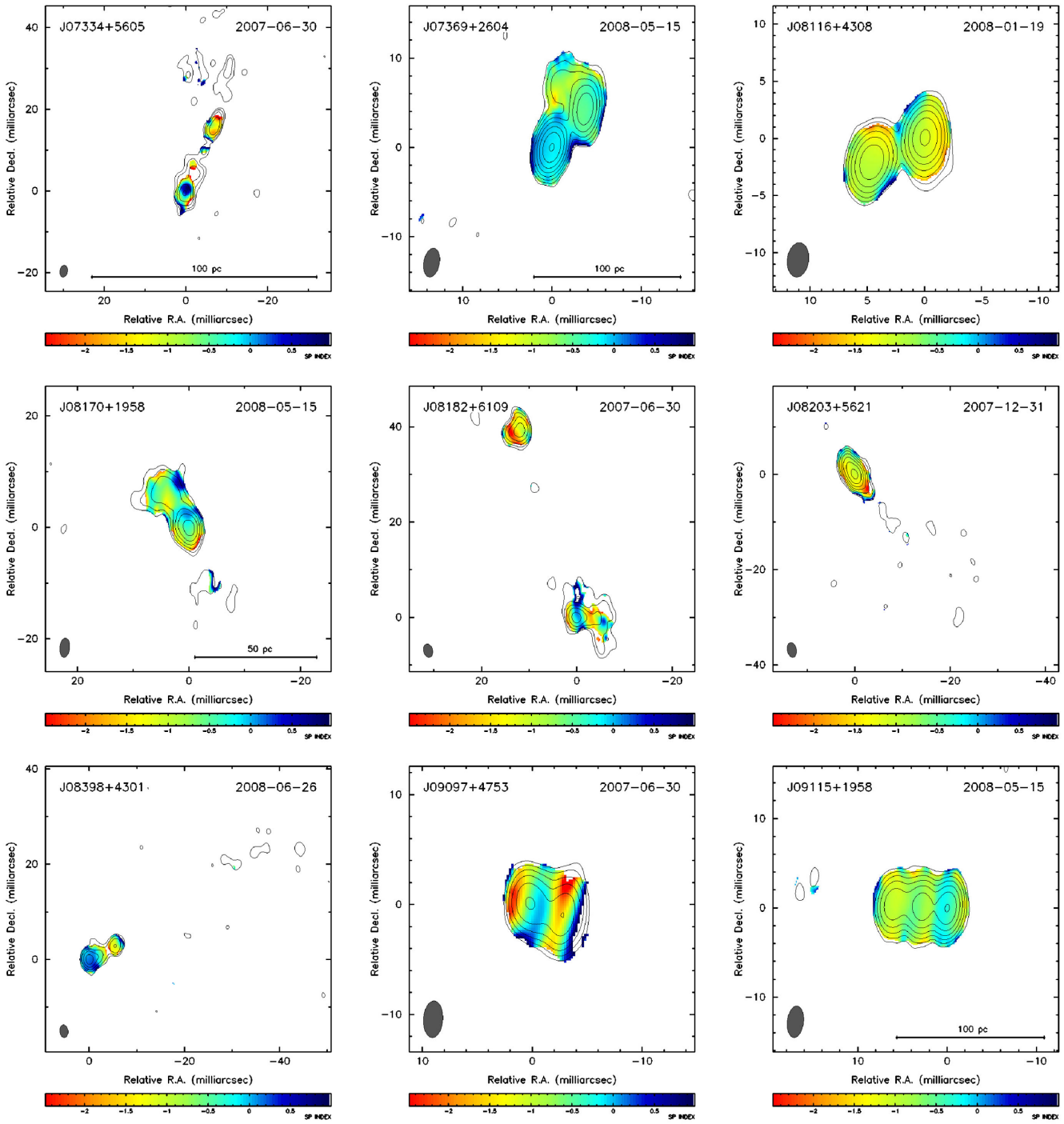

Figure 6. 5 GHz contour maps of refuted CSOs with 5–8 GHz spectral index map overlays. The contour levels begin at thrice the theoretical noise (typically ∼ 0.4 mJy for BT088 and 1.0 mJy for BT094) and increases by powers of 2. The colour scale is fixed from −2.5 to 1 to facilitate comparison. Sources with confirmed spectral redshifts have associated distance bars for linear scale. [The complete figure is available online.]

diffuse jets extend out to the west and east, respectively, creating an 'S-shaped' symmetry observed in other CSOs (e.g. 2352+495, Readhead et al. 1993; 1946+708, Taylor et al. 2009). No edge brightening is visible in this source, and it is not obvious where the jets terminate due to the FR-I morphology. As mentioned in Section 3.2, the non-instantaneous SED (Fig. 8) suggests possible extended emission. Liuzzo et al. (2013) characterized the source as a compact source with two sides lobes with extensions to the south.

4.2.14 J12279+3635

This source extends 453 pc from end to end. At the eastern edge of the source there is a bright, edge-brightened, steep-spectrum component with multiple smaller components tracing back towards the west, likely knots within a jet (Fig. 2N). An unresolved, flat-spectrum component, potentially the core, is then encountered followed by a weak, diffuse component bracketing the west side. This source was part of COINS (Peck & Taylor 2000) where it was

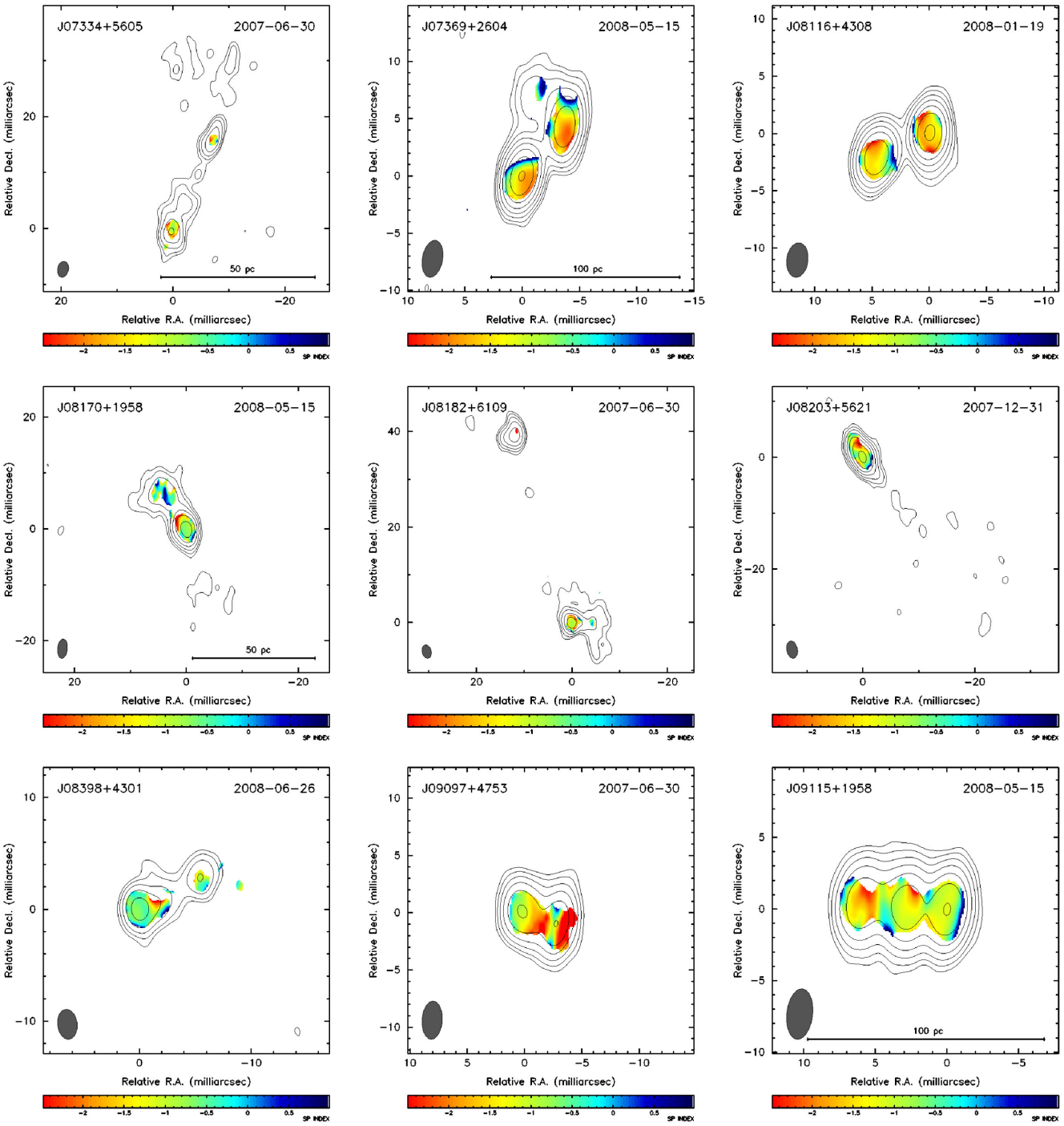

Figure 7. 5 GHz contour maps of refuted CSOs with 8–15 GHz spectral index map overlays. The contour levels begin at thrice the theoretical noise (typically $\sim$ 0.4 mJy for BT088 and 1.0 mJy for BT094) and increases by powers of 2. The colour scale is fixed from -2.5 to 1 to facilitate comparison. Sources with confirmed spectral redshifts have associated distance bars for linear scale. [The complete figure is available online.]

classified as a core-jet. Here, we reclassify this as a CSO based primarily on our identification of the core, and the observed emission in each lobe. The source was also studied by Dallacasa et al. (2013) where they claim the source has a core 32 mas from the edge brightening or the jet. We believe they were in fact referring to the western-most knot of the eastern jet instead of the much fainter core.

4.2.15 J12342+4753

The reasonably compact, flat- to steep-spectrum($\alpha_{5-8} \sim -0.5$ and $\alpha_{8-15} \sim -1.0$) core has a jet extending out to the north-west and a symmetric jet component to the south-east (Figs 2O and 3O). This is another example of a CSO with FR-I morphology in our sample.

Table 1. Confirmed VIPS compact symmetric objects Column 1: Source Name; Column 2 Date of observations; Column 3: Redshift of source; Column 4: Whether or not a core was observed; Column 5: Whether or not the source has 'FR-I-like morphology; Column 6: Whether or not this is an SBBH Candidate; Column 7–9: 5, 8, and 15 GHz integrated flux; Column 10: The extent of the source as determined by model fitting; Column 11: The calculated luminosity based on 5 GHz flux; Col 12: The ratio of the integrated fluxes of the brighter lobe over the dimmer lobe for each source; Column 13: The ratio of the length of the brighter jet over the length of the dimmer jet; Column 14: The angle subtended between the jets; Column 15: The object type as per NED where 'G' is galaxy, 'QSO' is quasar, 'VisS' is an object with visible data but no designation and '-' only has radio data and no designation.

Source	Date	z	Core	FR-I	SBBH cand.	$S_{5\,\mathrm{GHz}}$ (Jy)	$S_{8\,\mathrm{GHz}}$ (Jy)	$S_{15\,\mathrm{GHz}}$ (Jy)	Size (pc)	$L_{5\,\mathrm{GHz}}$ (W Hz^{-1})	Flux ratio	Arm ratio	Angle (°)	Object type
VIPS J07414+2706	2006 September 19	0.77[1]	Y	N	N	0.578	0.418	0.270	104.8 ± 0.0	1.50E27	19.35	1.02	159.2	VisS
VIPS J07542+5324	2007 December 31	0.84⋆	N	N	N	0.185	0.083	ND	?	5.98E26	1.33	?	?	–
VIPS J09062+4636	2007 December 31	0.0848[2]	Y	Y	N	0.113	0.126	0.121	61.6†	1.90E24	?	?	?	G
VIPS J09432+1702	2008 May 16	1.598[3]	Y	N	N	0.269	0.253	0.185	113.4	4.32E27	2.52	3.26	138.5	QSO
VIPS J10351+5628	2007 June 30	0.45[4]	N	N	N	1.021	0.714	0.233	187.9	7.15E26	1.32	?	?	G
VIPS J10426+2949	2008 May 16	0.61⋆	Y	N	N	0.264	0.122	0.045	?	3.86E26	1.49	1.76	175.9	–
VIPS J11113+1955	2008 May 16	0.2991[5]	N	N	N	0.562	0.314	0.077	71.6	1.50E26	1.31	?	?	G
VIPS J11359+4258	2007 December 31	1.0⋆	N	N	N	0.332	0.155	ND	?	1.65E27	1.89	?	?	–
VIPS J11488+5924	2007 June 30	0.010751[6]	Y	Y	N	0.417	0.385	0.279	6.6	1.08E23	1.70	0.51	157.7	G
VIPS J11584+2450	2006 September 19	0.2016[7]	Y	N	N	0.723	0.441	0.202	88.3	7.95E25	2.62	0.54	164.8	G
VIPS J11598+5820	2007 December 31	1.278[1]	N	N	N	0.286	0.103	ND	514.8	2.63E27	1.50	?	?	G
VIPS J12043+5202	2007 December 31	0.01⋆	Y	N	N	0.213	0.107	ND	?	4.37E22	1.51	0.68	179.3	–
VIPS J12201+2916	2008 June 26	0.002068[8]	Y	Y	N	0.388	0.349	0.236	1.5	7.61E21	1.25	2.11	151.1	G
VIPS J12279+3635	2008 June 26	1.973[9]	N	N	N	0.610	0.296	ND	453.1	1.66E28	?	?	?	QSO
VIPS J12342+4753	2007 December 31	0.372349[10]	Y	Y	N	0.275	0.223	0.140	80.8	1.23E26	2.35	0.92	162.9	QSO
VIPS J12448+4048	2008 January 19	0.813[9]	Y	N	N	0.592	0.322	0.114	217.0	1.77E27	2.31	1.86	176.1	QSO
VIPS J12545+1856	2008 June 26	0.1145[11]	Y	N	N	0.107	0.102	0.095	8.4	3.43E24	1.13	0.80	159.0	G
VIPS J13113+1658	2008 May 16	0.03 ⋆	Y	N	N	0.303	0.202	0.092	?	5.77E23	5.76	1.23	172.7	VisS
VIPS J13262+3154	2008 May 16	0.36801[12]	Y	N	N	2.045	1.246	ND	285.4	8.93E26	1.59	1.84	173.5	G
VIPS J13354+5844	NF‡	0.59⋆	?	?	?	0.637◇	–	–	?	?	?	?	?	VisS
VIPS J14136+1509	2006 November 4	0.35⋆	Y	N	N	0.195	0.139	0.092	?	7.51E25	5.09	0.469	142.7	G
VIPS J14142+4554	NF‡	0.186[2]	?	?	?	0.171◇	–	–	?	?	?	?	?	G
VIPS J16449+2536	2006 September 19	0.588[1]	Y	N	N	0.383	0.271	0.152	187.0	5.12E26	3.69	1.31	178.8	VisS
VIPS J17003+3830	2008 January 19	0.23⋆	Y	N	N	0.152	0.078	ND	?	2.21E25	5.29	0.46	161.3	–

Notes. †Not measured by component separation.
‡No follow-up observations performed.
⋆Photometric redshift from SDSS.
◇Flux density value from VIPS.
(1) This work; (2) Falco, Kochanek & Munoz (1998); (3) Healey et al. (2008); (4) Aller, Aller & Hughes (1992); (5) Peck et al. (2000); (6) de Vaucouleurs et al. (1991); (7) Zensus et al. (2002); (8) Ackermann et al. (2011); (9) Xu et al. (1994); (10) Hewett & Wild (2010); (11) Owen, Ledlow & Keel (1995); (12) Holt, Tadhunter & Morganti (2008).

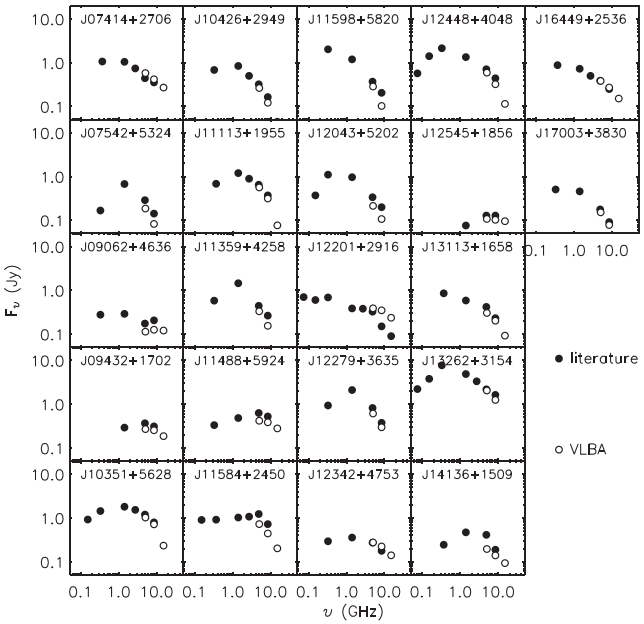

Figure 8. Plotting VLBA total flux for each CSO along with non-simultaneous VLA and single dish archival observations. This shows the spectral 'turnover' of each source, and also how much of the expected flux density (filled dots) we are recovering with our VLBA observations, which are marked by open dots.The archival fluxes in MHz are: 74 (VLSS; Cohen et al. 2007), 151 (6C; Hales et al. 1990), 325 (WENSS; Rengelink et al. 1997), 365 only used when no WENSS (TXS; Douglas et al. 1996), 1400 (NVSS; Condon et al. 1998), 2695 used only when no PKS (Condon & Dressel 1978), 2700 (PKS; Wall et al. 1975), 4850 (GB6; Gregory & Condon 1991), 8400 (CLASS; Myers et al. 2003). The only exception is for J1221+2916 which used Cohen et al. (2004) and Nagar, Falcke & Wilson (2005) for 74 and 15 000 MHz, respectively. Errors are smaller than the symbols in the plot.

4.2.16 J12448+4048

The flat-spectrum, compact core has apparent jet emission to the southwest terminating in a lobe (Figs 2P and 3P). A counter-lobe to the north-east and its luminosity and morphology suggest this lobe is directed away from us. This source was classified as CSO in COINS (Peck & Taylor 2000), and was the first quasar (QSO) classified as such.

4.2.17 J12545+1856

This compact source exhibits slight extensions to the east and west out of a compact, flat-spectrum centre (Figs 2Q and 3Q). This seems to be a very small (8.4 pc) CSO just resolved in these observations.

4.2.18 J13113+1658

The centre of this source is flat-spectrum and has jet emission to both the north and south (Figs 2R and 3R). This is a COINS source (Peck & Taylor 2000), but remained a candidate in that sample. Here, we classify this source as a CSO due to the centrally located flat-spectrum emission. Note that this source does not display the classic edge brightening of many other CSOs and instead belongs to the FR-I-like CSOs discussed in Section 4.4.

4.2.19 J13262+3154

This source is an archetypical example of a CSO. The compact, flat-spectrum core is centrally located between two large steep-spectrum lobes which each exhibit edge brightening (Fig. 2S). The extended emission then curves towards the southwest. An exceptional characteristic of this CSO is the detection of polarization in the north-western lobe (Fig. 9). This source was observed as part of the 2 cm survey, where Kellermann et al. (1998) described it as having CSO morphology despite their lack of detection of the core. Mantovani et al. (2013) found this source to depolarized between 15 GHz and 8 GHz with low fractional polarization.

4.2.20 J13354+5844

We did not perform follow-up observations on this source. This source was observed as part of the Caltech–Jodrell Bank flat-spectrum (CJF) survey (Pearson et al. 1998) and folded into VIPS and classified as a CSO candidate after the follow-up list was constructed. However, Stanghellini et al. (2009) have images confirming the CSO status of this source and analysis completed by Sokolovsky et al. (2011) also classified this source as CSO.

4.2.21 J14136+1509

This source is a peculiar CSO with a bent morphology. The core is identified as the flat-spectrum ($\alpha_{5-8} \sim 0.1, \alpha_{8-15} \sim -0.5$) component at roughly the centre of the source (Figs 2T and 3T). A jet heads southeast, while a steeper spectrum counter-jet bends around to the west. A spectroscopic redshift of this source has not been measured, so an exact size cannot be determined.

4.2.22 J14142+4554

This source was observed as part of the VIPS pilot project (Taylor et al. 2005) and did not get added to the follow-up observation list. This source has been previously confirmed as a CSO as part of COINS (Gugliucci et al. 2005) therefore for completeness, we include it in the list of VIPS CSOs.

4.2.23 J16449+2536

The core of this source is easily identified as the compact flat-spectrum component just east of the bright component in the centre of this source (Figs 2U and 3U). Symmetric S-shaped jets then emerge to the north and south, terminating in edge-brightened hotspots separated by ∼200 pc (Table 1).

4.2.24 J17003+3830

The compact flat-spectrum core of this source has lobes both to the east and west (Fig. 2V). The western lobe is notably brighter and closer to the core either due to geometric effects or interaction with the local environment (Table 1). The ∼30° deviation from linearity for the three components is consistent with environmental interaction.

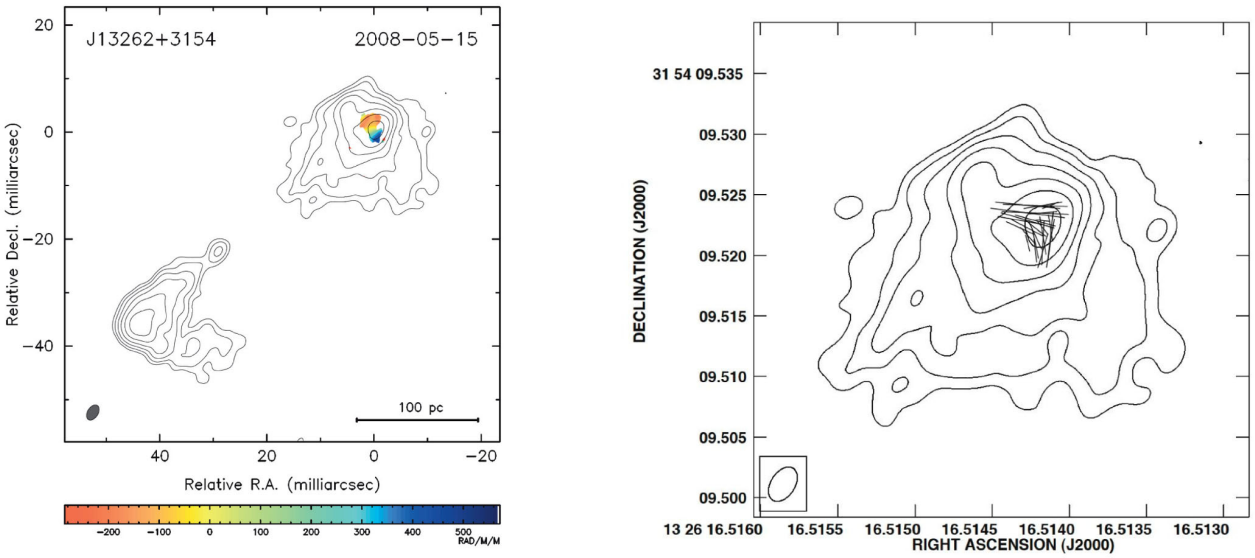

Figure 9. Left: the calculated rotation measure map of J13262+3154 generated from 5 and 8 GHz data overlaid on to 5 GHz contours. RMs of ∼−300 to 500 rad m^{-2} are observed with a notable sign change across the feature, corresponding to B-fields of ∼±0.06–2 μG assuming n_e of 0.1 cm^{-3} and an L of 0.3–10 parsec. Right: the corrected polarization angle of the magnetic fields (B) plotted on top of continuum for the north-western lobe. Contour levels begin at 2.0 mJy and increase by factors of $2^{\frac{1}{2}}$ in both images.

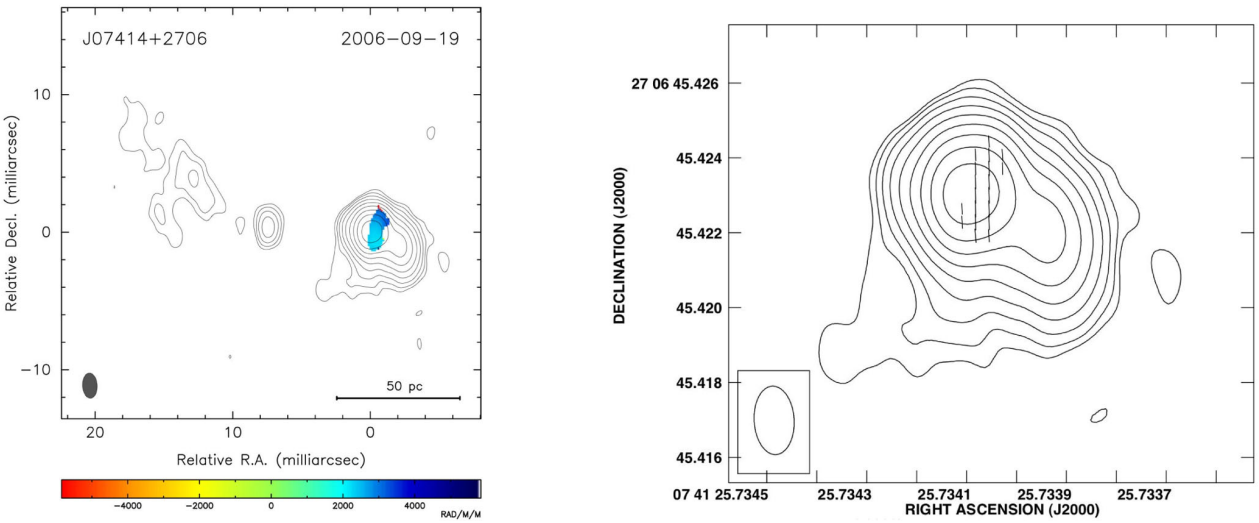

Figure 10. Left: the calculated Rotation Measure map of J07414+2706 generated from 8 and 15 GHz data overlaid on to 8 GHz contours. RMs of ∼1800–4000 rad m^{-2} are observed, corresponding to B-Fields of ∼±0.36–12 μG assuming n_e of 0.1 cm^{-3} and an L of 0.3–10 parsec. Right: the corrected polarization angle of the magnetic fields (B) plotted on top of continuum for the western lobe Contour levels begin at 0.45 mJy and increase by factors of $2^{\frac{1}{2}}$ in both images.

4.3 Remaining candidates and refuted CSOs

We were unable to either confirm or refute 33 of the candidates (Figs 4 and 5 and Table 2). Most of these sources, 16 out of 29, were not detected at 15 GHz which contributed to the high number of persisting candidates. The refuted CSO candidates are included for completeness in Figs 6 and 7 and Table 3 but further analysis past invalidating them as CSO candidates is outside the scope of this paper.

4.4 Morphology and luminosity

The connection between the morphology and other properties of radio galaxies was first revealed when Fanaroff & Riley (1974) took a sub-sample of the 3CR catalogue (Mackay 1971) and discovered a distinct luminosity cutoff (2.5×10^{25} W Hz^{-1} sr^{-1} at 178 MHz with an assumed $H_0 = 50\,\mathrm{km\,s^{-1}}$) separating diffuse sources whose highest flux was contained near the core (so-called FR-I sources) and edge-brightened sources that were most luminous where the jets terminated and ran into the surrounding medium (FR-II sources). While the canonical morphology of CSOs includes an edge-brightened lobe structure similar to what is observed in FR-II radio galaxies, several of the CSOs in this sample exhibit the more-diffuse, 'wispy' emission typically associated with the lower powered FR-I sources. Interestingly, when we plot the 5 GHz luminosity of each source in Fig. 11, an apparent separation of these morphologies by power is revealed (∼2×10^{25} W Hz^{-1}), just as for their much larger analogues. Using Fanaroff &

Table 2. Remaining VIPS CSO candidates Column 1: Source Name; Column 2: Date of observations; Column 3: Redshift of source; Column 4: whether or not this is an SBBH candidate; Columns 5–7: 5, 8, and 15 GHz integrated flux; Column 8: The extent of the source as determined by modefitting; Column 9: The calculated luminosity based on 5 GHz flux.

Source	Date	z	SBBH cand.	$S_{5\,\mathrm{GHz}}$ (Jy)	$S_{8\,\mathrm{GHz}}$ (Jy)	$S_{15\,\mathrm{GHz}}$ (Jy)	Size (pc)	$L_{5\,\mathrm{GHz}}$ (W Hz^{-1})
VIPS J07502+3119	2008 June 26	0.68⋆	N	0.072	0.033	ND	1675 ± 2	1.38E26
VIPS J07530+4231	NF‡	3.589 250[1]	N	0.398◇	–	–	101.7 ± 2.4	–
VIPS J08316+4608	2008 January 19	0.131 138[2]	Y	0.091	0.067	ND	25 ± 1	3.87E24
VIPS J08322+1832	2006 November 22	0.153[3]	N	0.484	0.369	0.226	36 ± 1	2.94E25
VIPS J08553+5751	NF‡	0.39⋆	N	0.119◇	–	–	?	–
VIPS J09452+2729	2008 January 19	0.68⋆	N	0.118	0.093	ND	76 ± 2	2.26E26
VIPS J10066+4836	2007 June 30	0.7⋆	Y	0.109	0.091	0.047	63 ± 2	2.24E26
VIPS J10320+5610	2007 December 31	1.0⋆	Y	0.111	0.060	ND	196 ± 3	5.53E26
VIPS J11106+4817	2007 December 31	0.74[4]	N	0.140	0.079	ND	242 ± 3	3.31E26
VIPS J11434+1834	2008 May 16	0.7⋆	Y	0.326	0.230	0.088	118 ± 2	6.70E26
VIPS J12018+3919	2008 January 19	2.37[5]	N	0.214	0.093	ND	427 ± 3	9.13E27
VIPS J12105+6422	2007 June 30	0.9⋆	Y	0.121	0.088	0.029	122 ± 3	4.64E26
VIPS J12152+1730	2008 May 16	0.268[6]	N	0.211	0.066	ND	559 ± 1	4.37E25
VIPS J12407+2405	2008 May 16	0.337[6]	N	0.278	0.167	0.079	232 ± 2	6.67E25
VIPS J12477+2551	2008 January 19	0.14⋆	Y	0.075	0.058	ND	31 ± 1	3.63E24
VIPS J13100+3403	2007 December 31	0.96⋆	N	0.104	0.050	ND	178 ± 3	4.68E26
VIPS J13136+5458	2007 February 19	0.613[7]	N	0.398	0.250	0.149	302 ± 2	5.92E26
VIPS J13199+3840	2008 January 19	0.45⋆	Y	0.117	0.077	ND	206 ± 2	8.19E25
VIPS J13222+2645	2008 June 26	0.53⋆	N	0.223	0.072	ND	165 ± 2	2.32E26
VIPS J13242+4048	NF‡	0.496[7]	N	0.365◇	–	–	118 ± 2	–
VIPS J13253+2109	2008 May 16	0.675[6]	Y	0.108	0.058	ND	110 ± 2	2.03E26
VIPS J13576+4353	2008 January 19	0.646[8]	Y	0.469	0.285	0.123	121 ± 2	7.93E26
VIPS J13586+4737	2007 December 31	0.23[7]	Y	0.295	0.201	0.105	36 ± 1	1.89E25
VIPS J14344+4236	2007 February 19	0.452[6]	N	0.304	0.194	0.075	196 ± 2	2.15E26
VIPS J14402+6108	2007 June 30	0.445[6]	N	0.113	0.064	ND	166 ± 2	7.70E25
VIPS J14426+3042	2008 June 26	1.0⋆	Y	0.144	0.064	ND	360 ± 3	7.17E26
VIPS J15136+2338	2008 May 16	0.218[6]	N	0.751	0.475	0.362	224 ± 1	9.72E25
VIPS J15590+5924	2007 June 30	0.0602[9]	N	0.118	0.094	ND	15 ± 1	1.94E22
VIPS J16022+2418	2008 January 19	1.788 871[10]	Y	0.181	0.131	0.060	463 ± 6	1.17E27
VIPS J16061+5521	2007 June 30	0.339[6]	N	0.077	0.043	ND	201 ± 2	2.75E25
VIPS J16087+1511	2008 May 16	0.94⋆	Y	0.091	0.077	0.043	123 ± 2	3.89E26
VIPS J16092+2641	2008 June 26	0.473[11]	N	1.5678	0.878	0.275	327 ± 2	1.24E27
VIPS J17309+3811	2008 June 26	?	N	0.169	0.099	ND	?	–

Notes. ‡No follow-up observations performed.
⋆Photometric redshift from SDSS.
◇Flux density value from VIPS.
(1) Abazajian et al. (2004); (2) Abazajian et al. (2003); (3) Adelman-McCarthy et al. (2008); (4) Hook et al. (1996); (5) Fanti et al. (2001); (6) This work; (7) Vermeulen et al. (1996); (8) Vermeulen et al. (2003); (9) Falco et al. (1998); (10) Hewett & Wild (2010); (11) NED (1992).

Riley's 178 MHz cutoff and ours yields a spectral index value, α, of -1.6 which is consistent with these lobe-dominated sources. A more stringent evaluation of these subsets using a two sample Kolmogorov–Smirnov (K–S) test cannot confirm these to be two independent populations, yielding p-value 0.059, which is just above the 0.050 cutoff typically used to constrain significance. This is not surprising given that these populations would overlap in luminosity and we observed only four CSOs with distinct FR-I morphology.

Overall, Fig. 11 also shows a strong relationship between the size of a source and its luminosity, with a Spearman correlation coefficient of 0.88 and an associated p-value of 1.36×10^{-5}. This could mean that the larger sources we observe are the more powerful ones that were able to expand further, or it could be due to them simply being older and having more time to fill their lobes with high-energy material. Fitting a power law to these data gives the relationship to be Size $\propto$ Luminosity$^{0.35}$.

It has been proposed that unlike traditional radio galaxies the difference in brightness between the two lobes of a CSO might be due more to interaction with the surrounding medium than simply orientation based boosting/deboosting (Saikia et al. 2001; Rossetti et al. 2006). When observed in large radio galaxies, the brighter lobe is typically further away from the core due to the time of arrival difference caused by one lobe being physically closer to us than the other. To investigate this, we measured the arm lengths of each lobe, R, using the distance from the core to the furthest model component in each lobe. We then plot the ratio of $R_{\mathrm{bright}}/R_{\mathrm{dim}}$ in Fig. 12, which will be greater than one for sources following the previously described scenario. While some sources certainly exhibit the expected behaviour, with a maximum ratio of 3.26, 7 of the 15 CSOs have hotspot length ratios less than unity, the smallest of which is 0.46. While projection effects could create such a result, it is more than plausible that this behaviour is due to interactions of these small jets with local inhomogeneities in their environment.

Table 3. Refuted VIPS CSO candidates Column 1: Source Name; Column 2 Date of observations; Column 3: Redshift of source; Column 4: Whether or not this is an SBBH Candidate; Columns 5–7: 5, 8, and 15 GHz integrated flux; Column 8: The calculated luminosity based on 5 GHz flux.

Source	Date	z	SBBH cand.	$S_{5\,\mathrm{GHz}}$ (Jy)	$S_{8\,\mathrm{GHz}}$ (Jy)	$S_{15\,\mathrm{GHz}}$ (Jy)	$L_{5\,\mathrm{GHz}}$ (W Hz^{-1})
VIPS J07334+5605	2007 June 30	0.104[1]	N	0.084	0.046	0.034	2.15E24
VIPS J07369+2604	2008 May 16	0.997[2]	N	0.234	0.205	0.149	1.16E27
VIPS J08116+4308	2008 January 19	?	N	0.150	0.086	0.047	–
VIPS J08170+1958	2008 May 16	0.138[3]	N	0.123	0.090	0.058	5.87E24
VIPS J08182+6109	2007 June 30	?	N	0.103	0.065	0.018	–
VIPS J08203+5621	2007 December 31	2.255⋆	N	0.143	0.069	0.036	5.39E27
VIPS J08398+4301	2008 June 26	0.22⋆	N	0.054	0.041	0.040	7.19E24
VIPS J09097+4753	2007 June 30	2.535⋆	N	0.090	0.066	0.033	4.52E27
VIPS J09115+1958	2008 May 16	1.635 343[4]	N	0.192	0.134	0.089	3.27E27
VIPS J09128+4422	2008 January 19	1.727[5]	N	0.164	0.129	0.087	3.21E27
VIPS J09267+2758	2006 September 19	0.22⋆	N	0.128	0.123	0.071	1.69E25
VIPS J09292+2536	2008 June 26	0.538 44[6]	N	0.108	0.086	0.110	1.17E26
VIPS J09355+3633	2007 December 31	2.858[7]	N	0.216	0.156	0.113	1.45E28
VIPS J10019+5540	2006 November 4	0.003 723[8]	N	0.075	0.075	0.048	2.77E21
VIPS J10051+2403	2008 June 26	0.17⋆	N	0.142	0.094	0.055	1.06E25
VIPS J10138+2449	2006 November 22	1.636[6]	N	0.816	0.925	0.660	1.39E28
VIPS J10225+3041	2008 June 26	1.319 802[4]	N	0.362	0.212	0.109	3.62E27
VIPS J10305+5132	2008 January 19	0.518 450[5]	N	0.102	0.077	0.038	1.01E26
VIPS J10509+3430	2008 May 16	2.52[9]	N	0.278	0.177	0.080	1.38E28
VIPS J10511+5347	2007 June 30	0.16⋆	N	0.199	0.127	0.048	1.29E25
VIPS J10512+4644	2008 January 19	1.419 418[4]	N	0.145	0.148	0.144	1.74E27
VIPS J10580+4248	2008 June 26	?	N	0.113	0.057	0.045	–
VIPS J11240+2336	2008 June 26	1.549[10]	N	0.278	0.257	0.280	4.14E27
VIPS J11285+3243	2008 January 19	0.369 528[6]	N	0.115	0.071	0.047	5.07E25
VIPS J11408+5912	2007 June 30	0.14⋆	N	0.192	0.128	0.053	9.31E24
VIPS J12009+2008	2008 June 26	?	N	0.198	0.219	0.193	–
VIPS J12035+4632	2006 November 4	0.14⋆	N	0.148	0.104	0.056	7.17E24
VIPS J12066+3941	2008 January 19	1.518 589[4]	N	0.308	0.329	0.296	4.36E27
VIPS J12074+2754	2007 February 19	2.182 064[4]	N	0.428	0.329	0.239	1.49E28
VIPS J12414+5458	2007 June 30	0.04⋆	N	0.129	0.070	0.026	4.42E23
VIPS J12582+5421	2007 June 30	?	N	0.225	0.088	0.024	–
VIPS J12595+5140	2006 November 22	0.405⋆	N	0.249	0.398	0.484	1.36E26
VIPS J13128+5548	2007 June 30	0.975⋆	N	0.209	0.131	0.036	9.79E26
VIPS J13223+4303	2007 December 31	0.07⋆	N	0.108	0.037	0.019	1.19E24
VIPS J14091+3642	2008 June 26	0.996[11]	N	0.190	0.101	0.050	9.38E26
VIPS J14489+5326	2007 December 31	0.58⋆	N	0.135	0.104	0.069	1.75E26
VIPS J14519+6357	2006 November 22	?	N	0.193	0.163	0.058	–
VIPS J15077+5857	2007 June 30	0.25⋆	N	0.166	0.134	0.034	2.94E25
VIPS J15159+2458	2006 September 19	0.151[12]	N	0.116	0.089	?	1.28E24
VIPS J15186+5002	2008 Janember 19	1.513 443[4]	N	0.073	0.055	0.034	1.02E27
VIPS J15451+4751	2007 December 31	1.277[13]	N	0.288	0.197	0.103	2.65E27
VIPS J15594+1624	2008 May 16	0.17⋆	N	0.181	0.118	0.051	1.35E25
VIPS J16002+1838	2008 June 26	2.404 66[14]	N	0.119	0.092	0.049	5.27E27
VIPS J16021+3326	2007 February 19	1.1[15]	N	1.406	1.115	0.732	8.91E27
VIPS J16048+1926	2006 November 4	0.35⋆	N	0.221	0.142	0.048	8.50E25
VIPS J16323+2643	2008 January 19	2.683 038[4]	N	0.124	0.110	0.076	7.15E27
VIPS J16325+3547	2006 November 22	0.07⋆	Y	0.237	0.141	0.050	2.61E24
VIPS J16538+3503	2007 December 31	0.57⋆	N	0.097	0.050	0.023	1.20E26
VIPS J16559+5430	2007 June 30	1.04[17]	N	0.132	0.122	0.060	7.27E26
VIPS J17073+4204	2007 December 31	?	N	0.123	0.052	0.022	–
VIPS J17233+3417	2008 May 16	0.206[18]	N	0.218	0.178	0.086	2.48E25
VIPS J17246+6055	2006 November 4	0.33⋆	Y	0.202	0.157	0.105	6.79E25

Notes. ‡No follow-up observations performed.
⋆Photometric redshift from SDSS.
◇Flux density value from VIPS.
(1) Marcha et al. (1996); (2) Healey et al. (2008); (3) Glikman et al. (2007); (4) Hewett & Wild (2010); (5) Abazajian et al. (2004); (6) Adelman-McCarthy et al. (2007); (7) Adelman-McCarthy et al. (2006); (8) Hagiwara, Klöckner & Baan (2004); (9) Hewitt & Burbidge (1989); (10) Ackermann et al. (2011); (11) Kunert-Bajraszewska & Marecki (2007); (12) This work; (13) Vermeulen & Taylor (1995); (14) Adelman-McCarthy et al. (2008); (15) Snellen et al. (2000); (16) Abazajian et al. (2005); (17) Véron-Cetty & Véron (2001); (18) Wills & Wills 1976.

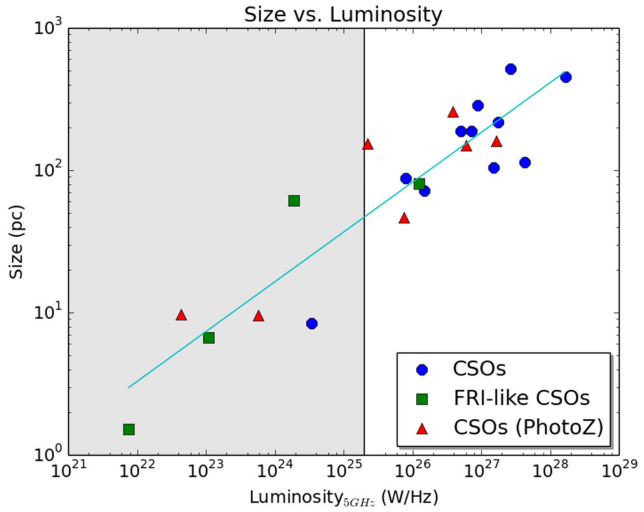

Figure 11. Here we plot the size of the CSOs from end to end (as determined by modelifting the data and looking at the separation between the components describing the edge of each jet) versus the 5 GHz luminosity. The blue circles represent archetypically 'edge-brightened' CSOs with reliable redshift data, the green squares represent the 'edge-darkened' FRI-like CSOs, and the red triangles the 'edge-brightened' CSOs where we had to use SDSS photometric redshift data to calculate the size and luminosity. The grey region of the plot indicates a luminosity less than 2×10^{25} W Hz^{-1}, our imposed cut between FR-I and FR-II morphology. A power law, with an index of 0.35, was fit to these data and is plotted in cyan.

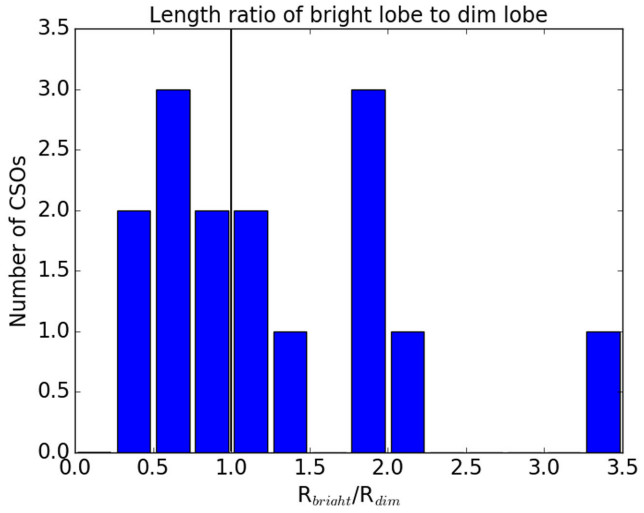

Figure 12. A histogram, with bin widths of 0.25, of the ratio of the arm length of the brighter lobe divided by the arm length of the dimmer one. The ratios less than 1 (indicated by the black line) might represent significant interaction with the local environment, causing the foreshortening of the typically longer, bright arm.

4.5 CSO polarization

As mentioned in Section 3.3, two of these CSOs have detections of polarized emission. In both of these sources, we observed the polarized flux in the brighter lobe of the source. This is consistent with Gugliucci et al. (2007), where polarization results for another two confirmed CSOs were reported, which also detected polarized emission only in the brighter lobe. They also found unusually high flux ratios (10 and 14) for the lobes of these CSOs, whereas only one of ours is high (19 and 1.6 in J07414+2706 and J13262+3154, respectively, while the median of the distribution is 1.79). This is consistent with the AGN unification scenario where the emission of most CSOs is depolarized as it passes through the dusty circumnuclear torus on its way to us, but for a few tilted CSOs (where one of the lobes would appear significantly brighter) the emission from the end of the near lobe does not pass through the torus on its path towards us.

The three IF pairs that detected stronger polarization in each source were used to compute rotation measures (RMs) as a function of position (Figs 9 and 10) wherever polarization was detected at all three pairs by fitting the change in polarization angle (β) to $RM = \frac{\beta}{\lambda^2}$, with values ranging from 1800 to 4000 and -300 to 500 rad m^{-2} for J07414+2706 and J13262+3154, respectively. The RM is dependent on the magnetic field ($\vec{B}$) and the electron number density (n_e) by:

$$RM = \frac{e^3}{2\pi m_e^2 c^4} \int_0^L n_e \boldsymbol{B} \cdot \mathrm{d}\boldsymbol{s} \quad (1)$$

where L is the path length of the Faraday screen, e and m_e are the charge and mass of the electron and c is the speed of light. These rotation measures were then used to calculate the magnetic field polarization angle corrected for Faraday rotation and are plotted on the right side of each figure. Following the assumptions of Gugliucci et al. (2007) and the references therein (specifically Stauffer & Spinrad 1979), if we assume $n_e = 1100 \pm 350$ cm^{-3}, and lower and upper limits for L of 0.3 and 10 pc, we calculate magnetic fields of 0.21 to 16 and 0.04 to 2.7 μG for J07414+2706 and J13262+3154, respectively.

Here, we point out the sign change in RM from one side of the polarized feature of J13262+3154 to the other, which could indicate a reversal of the magnetic field as seen in the above equation. However, since the polarized region is not well resolved (less than 3 beams across), it does not satisfy the requirements for an RM gradient outlined in Taylor & Zavala (2010) and therefore is not strong evidence for a magnetic field reversal in this source.

4.6 High-energy emission from CSOs

Despite theoretical expectations that CSOs might be isotropic γ-ray emitters, presumably due to inverse Compton scattering within the lobes of these compact sources (e.g. Stawarz et al. 2008) none of our CSOs have been detected by telescopes such as the *Fermi Gamma-ray Space Telescope*. This is well matched with empirical results from other CSOs, with in fact only one candidate being detected by *Fermi* to date (Müller et al. 2014). It is still possible these sources are emitting γ-rays via conventional means and that these are being beamed in the direction of the jets. In fact, it is quite possible that some of the blazars detected by *Fermi* have a physical extent less than 1 kpc, but this information is impossible to disentangle.

4.7 Incidence of CSOs

Using the number of confirmed CSOs as a lower limit and adding in the remaining candidates for an upper limit, we have 24–57 CSOs within the VIPS catalogue of 1127 sources (2.1–5.1 per cent). While the spectral and flux density prerequisites imposed on the VIPS sample limit what can be surmised about the fraction of CSOs within the entire population of radio-loud AGN, this is the most complete sample to date to investigate the CSO population. Comparing this with other samples and supersets, Peck & Taylor (2000) report CSO incidences of 11 per cent, 4.4 per cent and 2.1 per cent for PR,

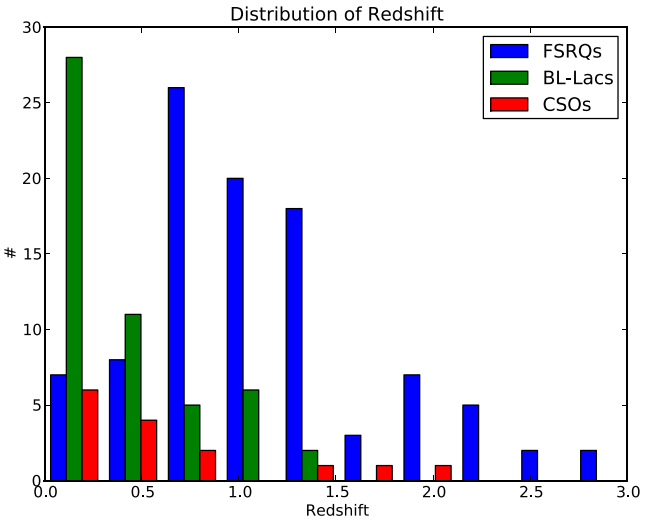

Figure 13. Here the redshift (z) distribution of the CSOs with reliable redshift data are plotted along with the distribution of redshifts for FRSQs and Bl-Lac object is plotted for comparison. While the CSOs and FSRQs are clearly different distributions, possibly due to selection effects, the same cannot be said for CSOs and BL-Lacs.

PR+CJ, and PR+CJ+VCS, where PR, CJ and VCS are Pearson-Readhead survey (Pearson & Readhead 1988), the Caltech–Jodrell Bank survey (Taylor et al. 1994) and the VLBA Calibrator Survey (Peck & Beasley 1998), respectively. Direct comparison of these numbers is difficult since each sample had independent selection criteria and the follow-up analysis, particularly of the VCS, was not always rigorous. Peck & Taylor speculated that the CSO fraction was inversely related to the limiting flux density of the survey, with PR having a cutoff of 1.3 Jy at 5 GHz, compared to just 0.1 Jy at 5 GHz for the VCS. The VIPS survey has a limiting flux density of 0.085 Jy at 8 GHz (Helmboldt et al. 2007), comparable to VCS, yet has a CSO fraction closer to that of PR+CJ. It seems likely that the VCS survey was deficient in CSOs due to its worse imaging characteristics. The high CSO fraction in the PR survey can be explained as a fluke of small number statistics.

The redshift distribution of VIPS CSOs (Fig. 13) shows a decay in incidence with redshift. This may be mostly due to selection effects, since although the emission from CSOs is bright, it is by definition not strongly beamed towards us and therefore not doppler boosted. When compared to the redshift distribution of *Fermi* detected flat spectrum radio quasars (FSRQs) and BL-Lacertae objects (BL-Lacs), which seem to be representative samples of those types of sources, we see that the VIPS CSOs and *Fermi* FSRQs almost certainly come from independent populations with a two sample K–S test p-value of 3.25×10^{-12}. It is important to point out that this could either be due to selection effects or inherent characteristics of the populations. The same cannot be said for CSOs and BL-Lacs, with a K–S test p-value of 0.49, meaning we cannot rule out the possibility these are from a similar population distribution.

4.8 VIPS SBBH candidates

These multifrequency follow-up observations were additionally searched for either of the following.

(i) Two distinct flat- or inverted-spectrum compact cores.
(ii) Jet structure that cannot be easily traced back to a single point of origin.

We were unable to confirm any new SBBHs with these follow-up observations, and none of the 15 remaining candidates are particularly promising (see Figs 2–7). Making the assumption that no SBBHs were observed in VIPS, then from the combined VIPS and Caltech–Jodrell Bank flat-spectrum (CJF) sample together only one SBBH (0402+379; Rodriguez et al. 2006) has been detected out of 1279 sources. Reconciling this within the current merger driven paradigm of galaxy evolution minimally requires that our understanding of black hole merger times, particularly the so-called final parsec problem of the merger stalling for small radii (Merritt 2006), be re-evaluated. This is consistent with Burke-Spolaor (2011) result of finding only a single SBBH within a sample of 3114 AGN with VLBI observations, which was also 0402+379. The detailed analysis within that paper of the 1575 sources with redshift data suggest that black hole binaries do not stall indefinitely at any radius <500 parsecs unless the most pessimistic estimates of merger rates hold true.

5 CONCLUSIONS

We have identified 24 CSOs within the VIPS sample using the spectral and morphological characteristics of each source, 15 of which were previously unclassified, and are still left with a remaining 33 CSO candidates (2–5 per cent of VIPS). Subsequent 15 GHz observations using higher bandwidth ($\geq$2 GHz) should confirm or deny at least half of the remaining candidates. Our sample of CSOs is large enough to observe an FR-I/FR-II distinction in both luminosity and morphology, similar to larger radio galaxies, which has not been previously identified. Correlation is observed within these data between the size and luminosity of CSOs, which could result either from pile-up of emitting material if the larger sources are also older or could indicate the ability of more powerful sources to expand more efficiently within their environments. Further evidence of the significance of environmental interaction with CSO jets is given by $\sim$1/2 of the CSOs having arm length ratios of the bright lobe divided by the dim lobe less than unity.

Polarization was detected in two of these CSOs, doubling the number of known polarized CSOs. In all four of these cases, polarization was only detected in the brighter lobe/jet and it was usually (3/4) detected near the working surface of the jet. This, coupled with 3/4 of the sources having unusually high-luminosity ratios for the lobes ($\sim$10–19) is consistent with most of the inherently polarized emission from CSOs being depolarized by the dusty molecular torus surrounding the nucleus, and only the sources that are oriented out of the plane of the sky enough to attain a line of sight to the end of the jets that does not pass through the torus being observed to be polarized.

Our lack of new SBBH detections is consistent with other comparable work, and indicates either that the 'final parsec' problem does not exist or that the more pessimistic projections of merger event rates could be correct.

ACKNOWLEDGEMENTS

The authors thank Mike Shaw for assistance with the HET observations and data analysis. Additionally, we thank Craig Walker, Trish Henning, Ylva Pihlström and Yuri Kovalev for numerous suggestions about how to improve this work, which have produced a more rigorous and robust paper. ST would also like to thank Justin Linford for enlightening discussions that improved this work greatly. The authors would also like to thank the anonymous referee, who contributed to the clarity of this work.

The HET is a joint project of the University of Texas at Austin, the Pennsylvania State University, Stanford University, Ludwig-Maximillians-Universität München, and Georg-August-Universität Göttingen. The HET is named in honor of its principal benefactors, William P. Hobby and Robert E. Eberly. The Marcario Low-Resolution Spectrograph (LRS) is named for Mike Marcario of High Lonesome Optics, who fabricated several optics for the instrument but died before its completion; it is a joint project of the HET partnership and the Instituto de Astronomía de la Universidad Nacional Autónoma de México. This research has made use of the NASA/IPAC Extragalactic Database (NED) which is operated by the Jet Propulsion Laboratory, California Institute of Technology, under contract with the National Aeronautics and Space Administration. The National Radio Astronomy Observatory is a facility of the National Science Foundation operated under cooperative agreement by Associated Universities, Inc. This research was partially conducted by the Australian Research Council Centre of Excellence for All-sky Astrophysics (CAASTRO), through project number CE110001020.

REFERENCES

Abazajian K. et al., 2003, AJ, 126, 2081
Abazajian K. et al., 2004, AJ, 128, 502
Abazajian K. et al., 2005, AJ, 129, 1755
Ackermann M. et al., 2011, ApJ, 743, 171
Adelman-McCarthy J. K. et al., 2006, ApJS, 162, 38
Adelman-McCarthy J. K. et al., 2007, ApJS, 172, 634
Adelman-McCarthy J. K. et al., 2008, ApJS, 175, 297
Aller M. F., Aller H. D., Hughes P. A., 1992, ApJ, 399, 16
Augusto P., 2009, Astron. Nachr., 330, 190
Augusto P., Gonzalez-Serrano J. I., Perez-Fournon I., Wilkinson P. N., 2006, MNRAS, 368, 1411
Becker R. H., White R. L., Edwards A. L., 1991, ApJS, 75, 1
Becker R. H., White R. L., Helfand D. J., 1995, ApJ, 450, 559
Bietenholz M. F., Kassim N., Frail D. A., Perley R. A., Erickson W. C., Hajian A. R., 1997, ApJ, 490, 291
Burke-Spolaor S., 2011, MNRAS, 410, 2113
Cohen A. S. et al., 2004, BAAS, 36, 91.05
Cohen A. S., Lane W. M., Cotton W. D., Kassim N. E., Lazio T. J. W., Perley R. A., Condon J. J., Erickson W. C., 2007, AJ, 134, 1245
Condon J. J., Dressel L. L., 1978, ApJ, 221, 456
Condon J. J., Cotton W. D., Greisen E. W., Yin Q. F., Perley R. A., Taylor G. B., Broderick J. J., 1998, AJ, 115, 1693
Dallacasa D., Orienti M., Fanti C., Fanti R., Stanghellini C., 2013, MNRAS, 433, 147
de Vaucouleurs G., de Vaucouleurs A., Corwin H. G., Jr, Buta R. J., Paturel G., Fouque P., 1991, Third Reference Catalogue of Bright Galaxies. Springer-Verlag, New York
de Vries N., Snellen I. A. G., Schilizzi R. T., Mack K.-H., Kaiser C. R., 2009, A&A, 498, 641
Douglas J. N., Bash F. N., Bozyan F. A., Torrence G. W., Wolfe C., 1996, AJ, 111, 1945
Falco E. E., Kochanek C. S., Munoz J. A., 1998, ApJ, 494, 47
Fanaroff B. L., Riley J. M., 1974, MNRAS, 167, 31P
Fanti C., Pozzi F., Dallacasa D., Fanti R., Gregorini L., Stanghellini C., Vigotti M., 2001, A&A, 369, 380
Glikman E., Helfand D. J., White R. L., Becker R. H., Gregg M. D., Lacy M., 2007, ApJ, 667, 673
Graham A. W., Scott N., 2015, ApJ, 798, 54
Gregory P. C., Condon J. J., 1991, ApJS, 75, 1011
Greisen E. W., 2003, in Heck A., ed., Astrophysics and Space Science Library, Vol. 285, Information Handling in Astronomy - Historical Vistas. Kluwer, Dordrecht, p. 109
Gugliucci N. E., Taylor G. B., Peck A. B., Giroletti M., 2005, ApJ, 622, 136
Gugliucci N. E., Taylor G. B., Peck A. B., Giroletti M., 2007, ApJ, 661, 78
Hagiwara Y., Klöckner H.-R., Baan W., 2004, MNRAS, 353, 1055
Hales S. E. G., Masson C. R., Warner P. J., Baldwin J. E., 1990, MNRAS, 246, 256
Healey S. E. et al., 2008, ApJS, 175, 97
Helmboldt J. F. et al., 2007, ApJ, 658, 203
Hewett P. C., Wild V., 2010 MNRAS, 405, 2302
Hewitt A., Burbidge G., 1989, ApJS, 69, 1
Hill G. J., MacQueen P. J., Nicklas H., Cobos D. F. J., Tejada C., Mitsch W., Wolf M. J., 1998, BAAS, 30, 1262
Holt J., Tadhunter C. N., Morganti R., 2008, MNRAS, 387, 639
Hook I. M., McMahon R. G., Irwin M. J., Hazard C., 1996, MNRAS, 282, 1274
Kellermann K. I., Vermeulen R. C., Zensus J. A., Cohen M. H., 1998, AJ, 115, 1295
Kormendy J., Ho L. C., 2013, ARA&A, 51, 511
Kunert-Bajraszewska M., Marecki A., 2007, A&A, 469, 437
Linford J. D. et al., 2011, ApJ, 726, 16
Liuzzo E. Buttiglione S., Giovannini G., Giroletti M., Capetti A., Taylor G. B., 2013, A&A, 550, A76
Mackay C. D., 1971, MNRAS, 154, 209
Magorrian J. et al., 1998, AJ, 115, 2285
Mantovani F., Rossetti A., Junor W., Saikia D. J., Salter C. J., 2013, A&A, 555, A4
Marcha M. J. M., Browne I. W. A., Impey C. D., Smith P. S., 1996, MNRAS, 281, 425
Merritt D., 2006, ApJ, 648,
Merritt D., Milosavljević M., 2005, Living Rev. Relativ., 8, 8
Müller C. et al., 2014, A&A, 562, AA4
Myers S. T. et al., 2003, MNRAS, 341, 1
Nagar N. M., Falcke H., Wilson A. S., 2005, A&A, 435, 521
NED11 1992, Redshift Obtained From Literature by The NED Team Prior to November 1992. p. 1
O'Dea C. P., 1998, PASP, 110, 493
Oke J. B., 1990, AJ, 99, 1621
Owen F. N., Ledlow M. J., Keel W. C., 1995, AJ, 109, 14
Pearson T. J., Readhead A. C. S., 1988, ApJ, 328, 114
Pearson T. J. et al., 1998, in Zensus J. A., Taylor G. B., Wrobel J. M., eds, ASP Conf. Ser. Vol. 144, IAU Colloq. 164: Radio Emission from Galactic and Extragalactic Compact Sources. Astron. Soc. Pac., San Francisco, p. 17
Peck A. B., Beasley A. J., 1998, in Zensus J. A., Taylor G. B., Wrobel J. M., eds, ASP Conf. Ser. Vol. 144, IAU Colloq. 164: Radio Emission from Galactic and Extragalactic Compact Sources. Astron. Soc. Pac., San Francisco, p. 155
Peck A. B., Taylor G. B., 2000, ApJ, 534, 90
Peck A. B., Taylor G. B., Fassnacht C. D., Readhead A. C. S., Vermeulen R. C., 2000, ApJ, 534, 104
Readhead A. C. S., Xu W., Pearson T. J., Wilkinson P. N., Polatidis A., 1993, BAAS, 25, 891
Readhead A. C. S., Taylor G. B., Pearson T. J., Wilkinson P. N., 1996, ApJ, 460, 634
Rengelink R. B., Tang Y., de Bruyn A. G., Miley G. K., Bremer M. N., Roettgering H. J. A., Bremer M. A. R., 1997, A&AS, 124, 259
Rodriguez C., Taylor G. B., Zavala R. T., Peck A. B., Pollack L. K., Romani R. W., 2006, ApJ, 646, 49
Rodriguez C., Taylor G. B., Zavala R. T., Pihlström Y. M., Peck A. B., 2009, ApJ, 697, 37
Rossetti A., Fanti C., Fanti R., Dallacasa D., Stanghellini C., 2006, A&A, 449, 49
Saikia D. J., Jeyakumar S., Salter C. J., Thomasson P., Spencer R. E., Mantovani F., 2001, MNRAS, 321, 37
Shepherd M. C., 1997, in Hunt G., H. E. Payne H. E., eds, ASP Conf. Ser. Vol. 125, Astronomical Data Analysis Software and Systems VI. Astron. Soc. Pac., San Francisco, p. 77
Shetrone M. et al., 2007, PASP, 119, 556
Sjouwerman L. O., Mioduszewski A. J., Greisen E. W., 2005, in Romney J., Reid M., eds, ASP Conf. Proc. Vol. 340, Future Directions in High Resolution Astronomy. Astron. Soc. Pac., San Francisco, p. 613

Snellen I. A. G., Schilizzi R. T., Miley G. K., de Bruyn A. G., Bremer M. N., Röumlttgering H. J. A., 2000, MNRAS, 319, 445
Snellen I. A. G., Mack K.-H., Schilizzi R. T., Tschager W., 2004, MNRAS, 348, 227
Sokolovsky K. V., Kovalev Y. Y., Pushkarev A. B., Mimica P., Perucho M., 2011, A&A, 535, A24
Stanghellini C., Dallacasa D., Venturi T., An T., Hong X. Y., 2009, Astron. Nachr., 330, 153
Stauffer J., Spinrad H., 1979, ApJ, 231, L51
Stawarz Ł., Ostorero L., Begelman M. C., Moderski R., Kataoka J., Wagner S., 2008, ApJ, 680, 911
Taylor G. B., Zavala R., 2010, ApJ, 722, L183
Taylor G. B., Vermeulen R. C., Pearson T. J., Readhead A. C. S., Henstock D. R., Browne I. W. A., Wilkinson P. N., 1994, ApJS, 95, 345
Taylor G. B., Wrobel J. M., Vermeulen R. C., 1998, ApJ, 498, 619
Taylor G. B., Marr J. M., Pearson T. J., Readhead A. C. S., 2000, ApJ, 541, 112
Taylor G. B. et al., 2005, ApJS, 159, 27
Taylor G. B., Charlot P., Vermeulen R. C., Pradel N., 2009, ApJ, 698, 1282
Tody D., 1986, in Crawford D. L., ed., Proc. SPIEConf. Ser. Vol. 627, Instrumentation in Astronomy VI. SPIE, Bellingham, p. 733
Tornikoski M. et al., 2009, Astron. Nachr., 330, 128
Tremblay S. E., Taylor G. B., Helmboldt J. F., Fassnacht C. D., Pearson T. J., 2008, ApJ, 684, 153
Tremblay S. E., Taylor G. B., Richards J. L., Readhead A. C. S., Helmboldt J. F., Romani R. W., Healey S. E., 2010, ApJ, 712, 159
Valdes F., 1992, in Worrall D. M., Biemesderfer C., Barnes J., eds, ASP Conf. Ser. Vol. 25, Astronomical Data Analysis Software and Systems I. Astron. Soc. Pac., San Francisco, p. 398
Vermeulen R. C., Taylor G. B., 1995, AJ, 109, 1983
Vermeulen R. C., Taylor G. B., Readhead A. C. S., Browne I. W. A., 1996, AJ, 111, 1013
Vermeulen R. C. et al., 2003, A&A, 404, 861
Véron-Cetty M.-P., Véron P., 2001, A&A, 374, 92
Wall J. V., Shimmins A. J., Bolton J. G., 1975, Aust. J. Phys. Astrophys. Suppl., 34, 55
Wilkinson P. N., Polatidis A. G., Readhead A. C. S., Xu W., Pearson T. J., 1994, ApJ, 432, L87
Wills D., Wills B. J., 1976, ApJS, 31, 143
Wright E. L., 2006, PASP, 118, 1711
Xu W., Lawrence C. R., Readhead A. C. S., Pearson T. J., 1994, AJ, 108, 395
Zensus J. A., Ros E., Kellermann K. I., Cohen M. H., Vermeulen R. C., Kadler M., 2002, AJ, 124, 662

SUPPORTING INFORMATION

Additional Supporting Information may be found in the online version of this article:

Figure 4. 5 GHz contour maps of the remaining CSO candidates with 5–8 GHz spectral index map overlays.
Figure 5. 5 GHz contour maps of the remaining CSO candidates with 8–15 GHz spectral index map overlays.
Figure 6. 5 GHz contour maps of refuted CSOs with 5–8 GHz spectral index map overlays.
Figure 7. 5 GHz contour maps of refuted CSOs with 8–15 GHz spectral index map overlays.
(http://www.mnras.oxfordjournals.org/lookup/suppl/doi:10.1093/mnras/stw592/-/DC1).

Please note: Oxford University Press is not responsible for the content or functionality of any supporting materials supplied by the authors. Any queries (other than missing material) should be directed to the corresponding author for the article.

This paper has been typeset from a TEX/LATEX file prepared by the author.